A central, shared role for disulfide bonds in Bacteroidota protein transport and gliding motility

Xiaolong Liu[1]*, Marieta Avramova[1], Justin C. Deme[2], Rachel L. Jones[1], Camilla A.K. Lundgren[1], Susan M. Lea[2]*, and Ben C. Berks[1]*

[1] Department of Biochemistry, University of Oxford, Oxford, United Kingdom.

[2] Center for Structural Biology, Center for Cancer Research, National Cancer Institute, Frederick, Maryland, United States of America.

* Corresponding authors. Email ben.berks@bioch.ox.ac.uk, susan.lea@nih.gov, xiaolong.liu@bioch.ox.ac.uk

Abstract

The gliding motility and Type 9 Secretion Systems (T9SSs) of Bacteroidota share a Power Chain that in current models uses a Hub complex to distribute energy to both the T9SS translocon and a moving gliding track. In *Flavobacterium johnsoniae* the cell surface gliding adhesins are attached to the internal gliding track by the outer membrane-spanning protein SprF. We show that both SprF and the T9SS component PorG contain twin-cysteine motifs that form a disulfide link to a shared cysteine residue in the Hub component GldK. These linkages are crucial for gliding motility and T9SS export, respectively. Since SprF moves with the gliding track, the SprF-GldK bond indicates that the Hub components are part of the gliding track in gliding Bacteroidota. We determine the structure of the 3 MDa Hub complex from the non-gliding bacterium *Porphyromonas gingivalis* and used this to model the *F. johnsoniae* gliding track.

25 ## Introduction

26 The phylum Bacteroidota (formerly Bacteroidetes) constitutes one of the largest
27 groups of Gram-negative bacteria. Bacteroidota are major human commensals and
28 anaerobic pathogens as well as being abundant members of the wider biosphere. Two
29 important phylum-specific features of the Bacteroidota are the ability to move using
30 gliding motility and to export proteins using the Type 9 Secretion System (T9SS).

31 The T9SS exports substrate proteins across the OM and plays key roles in
32 Bacteroidota virulence and nutrition[1-6]. During Type 9 transport the substrate protein
33 moves through a channel in the OM translocon protein SprA to from a complex with a
34 docked OM `carrier protein'[7](**Fig. 1a**). The resulting substrate-carrier protein complex
35 is then ejected from the translocon using an energetic input from a multi-protein Power
36 Chain[8]. T9SS substrates fall into two classes[9]. Type A substrates are extracted from
37 the translocon by the general carrier protein PorV and are subsequently either
38 released into the extracellular environment or covalently attached to cell surface
39 lipopolysaccharide[8,10]. By contrast, Type B substrates each have their own dedicated
40 carrier protein to which they remain bound thereby anchoring them to the cell
41 surface[11,12].

42 Gliding is the only mode of motility present in the Bacteroidota and allows rapid
43 movement across solid surfaces[5,13]. It is present in most free-living Bacteroidota and
44 some oral commensals and is mechanistically distinct from the gliding motility
45 exhibited by other phyla[13]. Bacteroidota gliding motility has been best studied in the
46 soil bacterium *Flavobacterium johnsoniae*. Gliding in this organism is mediated by the
47 cell surface adhesin SprB, which flows in helical trajectories up and down the cell[14-18].
48 When SprB adhesins attach to a solid surface the cell is propelled forward in a cork-

49 screwing motion[7,16,18,19]. The SprB adhesin is anchored to the cell surface by the OM
50 protein SprF [11,12,20](**Fig. 1a**). SprF is, in turn, thought to bind to a moving track structure
51 at the inner face of the OM resulting in the propulsion of the attached adhesin along
52 the cell body [16,21,22]. In current models of the gliding apparatus the track is
53 predominantly or exclusively a polymer of the OM-anchored lipoprotein GldJ[16,21,23].

54 Bacteroidota gliding has long been known to depend on the organism also
55 possessing a T9SS in order to transport gliding adhesins to the cell surface[24]. For
56 example, the *F. johnsoniae* adhesin SprB is a Type B T9SS substrate and SprF is its
57 cognate carrier protein[11,12]. More recently it has shown that gliding motility and Type 9
58 transport are intimately mechanistically linked because they are both powered by the
59 T9SS Power Chain[24-26]. In current models the Power Chain is composed of motor
60 complexes that transduce the energy of the inner membrane protonmotive force into
61 mechanical energy and transfer this across the periplasm to a Hub complex on the
62 inner face of the OM[25,27,28](**Fig. 1a**). The Hub complex then distributes this mechanical
63 energy both to the T9SS translocon and to the gliding machinery to power movement
64 of the gliding track[25]. In the non-gliding bacterium *Porphyromonas gingivalis* the Hub
65 has been shown to be a megadalton ring-shaped molecule composed of many copies
66 of the proteins PorK and PorN and anchored to the OM by the lipidated N-terminus of
67 PorK [24,29-31]. In the gliding bacterium *F. johnsoniae* the equivalent Hub proteins GldK
68 and GldN[32] are assumed to form a similar ring structure, the outer rim of which contacts
69 the gliding track[13,23]. The motors are envisaged to rotate the Hub ring (`pinion') to drive
70 the movement of the associated gliding track (`rack') [22,23].

71 Given the enormous mechanical forces exerted on the adhesins during gliding it
72 would be anticipated that the adhesin carrier protein SprF would form an extremely
73 strong interaction with the gliding track. However, AlphaFold3 (AF3) [33] fails to predict

a plausible complex between SprF and the presumed track protein GldJ. Intrigued by this observation we decided to investigate the nature of the interaction between SprF and the track. Our work uncovers an unanticipated and shared role for disulfide bonds in connecting gliding and T9SS components to the Hub proteins. This work leads to a radically new model for the organisation of the Power Chain in gliding bacteria in which the Hub proteins are components of the gliding track.

Results

A twin-cysteine motif in the periplasmic tail of SprF is essential for gliding motility

In considering how the adhesin carrier protein SprF might interact with the gliding track we noticed that the periplasmic C-terminal tail of SprF contains a Cys-Pro-Cys motif that is invariant in all close homologues (**Fig. 1b**). Since conserved cysteine residues often have a functional role, we examined whether this twin-cysteine motif is required for SprF to function in gliding motility. Substituting either or both of the cysteine residues abolished gliding (**Fig. 1c**). Thus, both cysteine residues are essential for SprF function. Control experiments confirmed that the cysteine substitutions do not affect the levels or stability of SprF (**Supplementary Data Fig. 1**).

SprF can be considered to carry out two mechanistically separable functions. First, it acts as a carrier protein for the export and surface-anchoring of the SprB adhesin. Second, it attaches to the periplasmic gliding tracks to allow movement of the attached adhesin. We used protease accessibility experiments to test whether the twin-cysteine

97 motif is required for SprF to fulfil its carrier protein function (**Fig. 1d**). In these
98 experiments a protease is added to the medium around the cells and digests any SprB
99 molecules present on the cell surface. However, if export of SprB is unable to take
100 place (for example in a Δ*sprF* background in **Fig. 1d**), the adhesin remains inside the
101 cell and is protected from digestion by the external protease. Using this approach, we
102 found substitution of the SprF cysteine residues either singly or in combination had no
103 effect on the surface localization of SprB (**Fig. 1d**). Thus, the twin-cysteine motif is not
104 required for the carrier protein function of SprF.

105 To determine whether the twin-cysteine motif is, instead, required for the interaction
106 of SprF with the gliding track we carried out live cell single molecule tracking
107 experiments (**Fig. 1e, Supplementary Video 1**). In this approach fluorophore-labelled
108 SprB adhesin molecules are tracked as a proxy for the behaviour of the SprF
109 molecules to which they are bound. In a wild-type SprF background a large proportion
110 of the SprB molecules move on sustained helical trajectories as previously
111 reported[15,17,18,25]. However, removing the cysteine pair in SprF almost completely
112 suppresses this continuous helical movement. Thus, the twin-cysteine motif is required
113 for SprF to make normal interactions with the gliding track. Although most of the SprB
114 molecules in the cysteine-substituted background were close to stationary, a minority
115 still exhibited short, apparently directed motions. 3D tracking confirmed that the
116 handedness of these short trajectories matched the exclusively left handed geometry
117 of the gliding tracks[15-17] showing that these trajectories still represent SprB molecules
118 moving on a track (**Extended Data Fig. 1**). The adhesins with these short trajectories
119 showed frequent stopping behaviour, often for extended periods of time (> 10
120 seconds). During these `stops' the molecules could be either immobile or slowly
121 diffusive, and the adhesin often resumed helical movement in a different direction from

122 the trajectory before the `stop'. Thus, SprF is still able to interact with the gliding tracks
123 in the absence of the twin-cysteine motif, but these residual interactions are sporadic,
124 short term, and prone to aberrant behaviour. Control experiments show that if SprB
125 export is blocked by the complete removal of SprF (Δ*sprF*) then the non-exported SprB
126 molecules in the periplasm exhibit rapid isotropic diffusion that is quite distinct from
127 the behaviours observed when the SprF cysteine residues are removed.

128

129 **SprF is disulfide-bonded to GldK**

130 Conserved cysteines residues in periplasmic proteins are often involved in forming
131 disulfide bonds. This prompted us to explore whether the twin-cysteine motif in SprF
132 was involved in forming a disulfide link to the gliding track. To do this we first trapped
133 the thiol/disulfide state of the cellular proteome by treating *F. johnsoniae* with the
134 membrane-permeable thiol-reactive reagent *N*-ethylmaleimide (NEM). NEM forms an
135 irreversible adduct with free thiol groups. The modified thiols are no longer able to
136 attack and break disulfide bonds and so the disulfide bonds present in the cell are
137 preserved.

138 Treatment of *F. johnsoniae* cells with NEM resulted in almost the entire SprF pool
139 being recovered in a high molecular mass adduct running larger than 100 kDa (**Fig.**
140 **2a**). Formation of this adduct was reversed by addition of the thiol-containing reagent
141 DTT, confirming that the two proteins were linked by a disulfide bond (**Fig. 2a**).
142 Formation of the adduct also required the presence of the twin-cysteine motif in SprF,
143 demonstrating the involvement of these residues in the disulfide linkage (**Fig. 2a**).

144 SprF anchors the gliding adhesin SprB to the cell surface. We found that SprB was
145 required for the formation of the SprF-containing disulfide adduct (**Fig. 2a**). The

146 disulfide adduct was also missing in a strain in which export of SprB was blocked by
147 deletion of the T9SS translocon (Δ*sprA* strain, **Fig. 2b**), though not by removal of a
148 T9SS carrier protein that is not involved in SprB export (Δ*porV* strain, **Fig. 2b**),
149 confirming that SprB must be exported and loaded onto SprF for disulfide bond
150 formation to occur.

151 The SprF adducts were still detected after dissipation of the protonmotive force that
152 powers the gliding apparatus[15,25] (**Extended Data Fig. 2a**). Thus, their stability does
153 not depend on active movement of the SprF-SprB complex.

154 To identify the partner protein to which SprF is disulfide linked we took a candidate
155 approach informed by our current understanding of the organisation of the gliding
156 motility apparatus. In this model the periplasmic domain of SprF interacts with a gliding
157 track constructed from GldJ protomers (**Fig. 1a**). Based on this model the partner
158 protein to which SprF is disulfide-linked should be GldJ. Surprisingly, however, no
159 adduct equivalent to that identified with SprF antibodies was detected by
160 immunoblotting against GldJ (**Fig. 2a**), thus ruling out GldJ as the binding partner of
161 SprF. Upon broadening our screen to other gliding components, we found that the
162 lipoprotein GldK was partially recovered in a disulfide-linked adduct with the same
163 molecular mass as that formed by SprF (**Fig. 2a**). Crucially this adduct was no longer
164 formed when the twin-cysteine motif of SprF was removed showing that the SprF is
165 the interacting partner (**Fig. 2a**). Thus, the Hub component GldK is the partner protein
166 to which SprF is disulfide linked. Because SprF is in continuous movement along the
167 gliding track, the covalent link between SprF and GldK implies that GldK is a
168 component of the track rather than being located in a separate Hub complex as
169 envisaged in the current gliding model (**Fig. 1a**).

170 We next attempted to identify the cysteine residue(s) in GldK that are involved in
171 forming the disulfide linkage with SprF. Discounting the lipidated N-terminal cysteine,
172 GldK contains two cysteine residues (Cys285 and Cys343). These cysteine residues
173 are highly conserved across GldK homologues (Fig. 3a). Gliding motility is blocked
174 when Cys343, but not Cys285, is substituted providing presumptive evidence that it is
175 Cys343 that forms the disulfide linkage with SprF (**Fig. 3b**). This is confirmed by
176 biochemical analysis which shows that the SprF-GldK disulfide bond is still present in
177 a *gldK*^{C285S} background but missing in a *gldK*^{C343S} strain (**Fig. 3c**). Export of the SprB
178 adhesin still takes place when the disulfide-bond forming Cys343 of GldK is
179 substituted, albeit with lower efficiency than in the wild-type strain (**Fig. 3d**).
180 Nevertheless, as with the SprF twin-cysteine deletion strain, single particle tracking
181 measurements fail to detect SprB molecules following the sustained helical trajectories
182 typical of gliding adhesins in wild-type cells. Although there are rare examples of
183 adhesins exhibiting short helical trajectories, most adhesins are close to stationary
184 (there is also a background of rapidly isotropically moving particles due to the elevated
185 levels of non-exported SprB molecules in the periplasm of this strain)(**Fig. 3e,**
186 **Supplementary Video 2**). Thus, for those adhesins that have been successfully
187 exported, the effects of removing GldK Cys343 on their mobility are equivalent to those
188 of removing the SprF twin-cysteine motif. This is as expected if these two groups of
189 cysteine residues are partners in the same disulfide bond.

190

191 **The SprF twin-cysteine residues have non-identical roles**

192 We next investigated the individual contributions of the two SprF Cys residues to
193 disulfide bond formation with GldK. Removing Cys326, but not Cys324, prevented

194 formation of the adduct with GldK (**Fig. 2a**). This shows that it is Cys326 that forms
195 the disulfide bond to GldK (**Fig. 3f**). Although the SprF-GldK disulfide bond still forms
196 when Cys324 is removed, the bond is only formed by a minority of the SprF molecules
197 present. This contrasts with the situation with the wild-type protein where almost the
198 entire SprF pool is crosslinked to GldK (**Fig. 2a**). Thus, Cys324 enhances the
199 efficiency of formation of the inter-protein disulfide bond. Our interpretation of this
200 observation is that Cys324 forms an intramolecular disulfide bond with Cys326, and
201 that this bond is then attacked by a cysteine thiol on GldK to form the SprF-GldK
202 disulfide link (**Fig. 3f**). Consequently, when this intramolecular disulfide bond is absent
203 in the SprF Cys324Ala variant, formation of the disulfide bond between the remaining
204 SprF cysteine and Cys343 in GldK requires an adventitious oxidant and so occurs with
205 low efficiency. We speculate that GldK is positioned sufficiently close to the OM that
206 periplasmic thiol oxidizing proteins are sterically occluded from accessing the
207 SprF/GldK interface to form the intrachain disulfide bond, and that to circumvent this
208 problem the cell introduces a 'donor' Cys324-Cys326 disulfide linkage into SprF during
209 its biosynthesis. The *F. johnsoniae* genome contains many periplasmic proteins with
210 potential thiol/disulfide interchange activity that could be involved in forming the initial
211 disulfide bond in SprF. Although none of these proteins have been implicated in gliding
212 function, a disulfide oxidoreductase termed TlpB has been shown to be required for
213 gliding motility in other Bacteroidota[34,35].

214 It is notable that the SprF-GldK adduct is present even without NEM treatment of
215 the bacteria in cells expressing the SprF Cys324A variant (**Fig. 2a**). This suggests that
216 Cys324 is responsible for the instability of the SprF-GldK disulfide linkage in wild-type
217 cells. Because NEM treatment of wild-type cells stabilises almost the entire SprF pool
218 in disulfide linked adducts with GldK (**Fig. 2a**), we can infer that under physiological

219 steady state conditions Cys324 is present almost exclusively in the thiol state
220 (derivatized by NEM) and so the Cys324-Cys326/Cys326-GldK disulfide equilibrium is
221 positioned heavily towards the Cys326-GldK side (**Fig. 3f**). This is intuitively
222 reasonable because the vicinal thiols in SprF are separated by only a single amino
223 acid residue and so the disulfide bond between them will be highly strained and
224 unstable relative to the Cys326-GldK disulfide. We interpret the need for NEM
225 treatment in our experimental analysis of disulfide bonding patterns as reflecting the
226 fact that SprF and GldK will irreversibly separate once solubilized in SDS if their
227 disulfide linkage is broken. Consequently, even very low levels of attack on the intra-
228 protein disulfide bond by Cys324 will, over time, remove the SprF-GldK adduct from
229 the sample. By contrast, in the cellular context SprF and GldK are kept adjacent
230 allowing their disulfide bond to be reformed if it is cleaved by Cys324.

231 Both of the cysteine residues in the C-tail of SprF are essential for gliding (**Fig. 1c**).
232 This behaviour is readily explained for Cys326 because this residue is required to form
233 the disulfide bond with GldK. However, this disulfide bond is still formed when Cys324
234 is absent, raising the question of why this residue is needed for the cell to move. One
235 possibility is that the small proportion of SprF molecules that are crosslinked to GldK
236 in this background (**Fig. 2a**) is insufficient to sustain gliding. A second possibility is that
237 the gliding mechanism requires the crosslink between Cys326 and GldK to be
238 dynamically reversible, but that this is no longer possible without Cys324 to attack the
239 intra-protein disulfide bond (**Fig. 3f**). In an attempt to gain insight into these
240 possibilities we examined the effect of the single SprF cysteine substitutions on the
241 mobility of fluorophore-labelled adhesins (**Fig. 1e**). As expected, removal of Cys326
242 phenocopies the behaviour of other backgrounds (*sprF*^{C324A,C326A}, *gldK*^{C343S}) that
243 cannot form the SprF-GldK disulfide bond (**Figs. 1e and 3e**). By contrast, removal of

244 Cys324 produces a mix of behaviours in which some adhesins perform sustained
245 helical movements (like cells with wild-type SprF) whilst others only move helically for
246 short periods (as in strains that cannot disulfide bond to GldK)(**Fig. 1e**), consistent with
247 the observation that only a proportion of the SprF molecules are disulfide-bonded to
248 the gliding track in these cells (**Fig. 2a**). If, as we hypothesise, the SprF-GldK disulfide
249 links in this strain cannot readily be reversed, then the fact that some adhesins
250 (presumably those with a GldK-linked SprF) are able to sustain continuous helical
251 movement for multiple circuits of the cell implies that the ability to break the disulfide
252 linkage is not a requirement for normal adhesin motion. This conclusion is
253 strengthened by the observation that the movement of another protein that moves on
254 the gliding track (SprC[36]) is unimpaired in the *sprF*^{C324A} background (**Fig. 1e**). Thus,
255 locking some SprF molecules to GldK does not impede the movement of the track
256 network.

257

258 **GldK Cys343 is required for Type 9 protein export**

259 The work detailed here has shown that Cys343 of GldK plays a crucial role in gliding
260 motility by forming a disulfide bond that attaches the SprF-SprB adhesin complex to
261 the gliding track. It is, therefore, very surprising that this cysteine residue is conserved
262 in the equivalent PorK protein of *P. gingivalis* even though this organism does not glide
263 and so does not need to interact with gliding adhesins (**Fig. 3a**). Indeed, this residue
264 is completely invariant across GldK/PorK proteins. This strongly suggests that this
265 conserved cysteine has a role(s) beyond anchoring adhesin carrier proteins. More
266 specifically, since PorK is part of the *P. gingivalis* T9SS[24], it suggests that the
267 conserved cysteine is involved in Type 9 protein export.

268 To test this hypothesis, we asked whether GldK Cys343 is required for Type 9 protein
269 secretion in *F. johnsoniae*. We found that removal of this residue completely abrogated
270 the export of a model T9SS Type A substrate protein (**Fig. 3g**). It also phenocopied
271 the effects of removing GldK or the T9SS translocon SprA on the secreted proteome,
272 which is dominated by Type A T9SS-secreted proteins[7] (**Fig. 3h**). By contrast, and as
273 noted previously above, removal of Cys343 reduces rather than completely blocks
274 export of the Type B T9SS substrate SprB (**Fig. 3d**). Thus, these experiments confirm
275 the hypothesis that GldK Cys343 is involved in Type 9 protein export in *F. johnsoniae*,
276 in addition to gliding motility, and that it is essential for the secretion of Type A
277 substrates. Control experiments using SprF variants lacking the twin-cysteine motif
278 confirm that the requirement for GldK Cys343 in Type 9 transport is independent of
279 the disulfide bond that GldK Cys343 makes with SprF (**Extended Data Fig. 3**).

280

281 **GldK Cys343 forms a disulfide bond with the T9SS component PorG**

282 Since the established mechanistic function of GldK Cys343 in gliding motility is to
283 form a disulfide bond with a cysteine in a partner protein (SprF), it is highly likely that
284 its role in Type 9 protein secretion is also to form a disulfide linkage with a partner
285 protein(s), in this case presumably a T9SS component. Indeed, a possible additional
286 disulfide-bonded GldK adduct could be distinguished after NEM treatment of cells as
287 a faint band in some high exposure GldK immunoblots. This is most clearly seen in
288 the example shown in **Extended Data Fig. 4.**

289 Analysis of known T9SS components identified the protein PorG as the most likely
290 candidate to partner GldK. *F. johnsoniae* PorG (Fjoh_1692, hereafter $PorG_{Fj}$) is
291 predicted to be an 8-stranded OM protein in which the periplasmic C-tail contains the

292 same vicinal Cys-Xaa-Cys motif used by SprF to form a disulfide bond with GldK (**Fig.**
293 **4a**). The presence of cysteine residues in the PorG tail is a conserved feature across
294 the T9SS-containing Bacteroidota, although the number, spacing, and positioning of
295 the residues varies (**Fig. 4a**). For example, *P. gingivalis* PorG (PG0189 in strain W83,
296 hereafter $PorG_{Pg}$) contains a single cysteine that aligns with the second cysteine in the
297 *F. johnsoniae* $PorG_{Fj}$ motif (**Fig. 4a**). $PorG_{Pg}$ was identified as an essential T9SS
298 component in *P. gingivalis*[37,38] but its mechanistic role is unknown. Importantly, $PorG_{Pg}$
299 has been reported to co-purify with the *P. gingivalis* PorKN Hub Complex[29], an
300 observation which is consistent with the hypothesis that PorG is a disulfide-linked
301 partner of GldK/PorK.

302 We constructed a *porG* deletion mutant in *F. johnsoniae* and used this to confirm
303 that PorG is part of the T9SS in this organism. Specifically, PorG is essential for the
304 secretion of both Type A substrates and the Type B substrate SprB (**Fig. 4b-d**). The
305 $porG_{Fj}$ deletion mutant was also unable to glide, consistent with its inability to export
306 the SprB glding adhesin (**Fig. 4e**). Control experiments confirmed that the absence of
307 $PorG_{Fj}$ did not affect cellular levels of the key T9SS and gliding components SprA
308 (T9SS translocon), GldK, or SprF (**Extended Data Fig. 5b**).

309 We next tested whether the C-tail Cys_{225}-Xaa-Cys_{227} motif was important for *F.*
310 *johnsoniae* PorG function. Type A protein export and gliding motility were fully blocked
311 in the absence of the cysteine pair (**Fig. 4b,d,e**). However, partial export of the Type
312 B substrate SprB still occurred (**Fig. 4c**). This is in contrast to the phenotype of a full
313 $PorG_{Fj}$ deletion (**Fig. 4c**) but is reminiscent of the phenotype obtained after deleting
314 the GldK Cys343 to which we propose $PorG_{Fj}$ binds (**Fig. 3d**). Removal of Cys225
315 alone was sufficient to almost completely block export of a model Type A substrate,
316 whereas removal of Cys227 had no substantive effect on this process (**Fig. 4b**),

317 indicating that Cys225 is the more important of the two cysteine residues. Export of
318 the Type B substrate SprB and gliding motility were either not (Cys227), or only slightly
319 (Cys225), sensitive to the loss of the individual cysteine residues (**Fig. 4d,e and**
320 **Extended Data Fig. 5a**). Overall, the phenotypic effects of Cys225 removal are more
321 severe than those of Cys227 loss.

322 Having established that the $PorG_{Fj}$ cysteine motif is required for $PorG_{Fj}$ function we
323 next investigated whether this motif was involved in forming the predicted interaction
324 with GldK Cys343. In order to detect $PorG_{Fj}$ by immunoblotting we introduced an
325 ALFA-tag into loop 3 of $PorG_{Fj}$. This epitope tag did not affect the expression, stability,
326 or functionality of $PorG_{Fj}$, and epitope-tagged cysteine motif variants showed the same
327 patterns of functional defects as the untagged proteins (**Extended Data Fig. 5c-e**).
328 Treatment of cells with NEM trapped a proportion of the $PorG_{Fj}$ molecules in a
329 disulfide-linked adduct (**Fig. 4f**) of the same size as the additional, non-SprF, adduct
330 of GldK detected in **Extended Data Fig. 4**. This adduct was absent in a *gldK* deletion
331 mutant (**Fig. 4f**) confirming that GldK is the partner protein to which $PorG_{Fj}$ is disulfide-
332 linked. Removal of GldK Cys343, but not Cys285, also blocked formation of the $PorG_{Fj}$
333 adduct confirming that GldK uses the same cysteine residue to form disulfide
334 crosslinks with both $PorG_{Fj}$ and SprF (**Fig. 4f**). Formation of the $PorG_{Fj}$-GldK adduct
335 required the presence of the twin-cysteine motif in $PorG_{Fj}$ demonstrating the
336 involvement of these residues in the disulfide linkage (**Fig. 4f**). When the $PorG_{Fj}$
337 cysteines are individually removed the adduct is still observed (**Fig. 4f**) indicating that
338 either of the cysteines can form a bond with GldK. Nevertheless, in both cases the
339 levels of the $PorG_{Fj}$-GldK adduct are lower than in the wild type, with the larger effect
340 of Cys225 removal suggesting that Cys225 is preferentially involved in forming the
341 inter-subunit disulfide bond in agreement with the greater functional importance of this

342 cysteine. Removal of either of the $PorG_{Fj}$ cysteine residues results in the $PorG_{Fj}$-GldK
343 adduct being detected even in the absence of NEM treatment (**Fig. 4f**) suggesting that
344 in these variants the disulfide bond with GldK is stabilised because it cannot be
345 attacked by the missing $PorG_{Fj}$ cysteine. Disulfide bond formation between PorG and
346 GldK does not require T9SS activity (**Extended Data Fig. 5f**).

347 Overall, the disulfide-bonding behaviours of the twin-cysteine motifs of $PorG_{Fj}$ and
348 SprF are comparable, although with $PorG_{Fj}$ there is less differentiation between the
349 roles of the two cysteines. Consequently, we interpret the behaviour of the $PorG_{Fj}$
350 cysteines in an analogous way to the SprF motif (**Fig. 3f**). Specifically, we envisage
351 that an intramolecular disulfide bond is formed between $PorG_{Fj}$ Cys225 and Cys227
352 during $PorG_{Fj}$ biogenesis, that this bond is subsequently attacked by GldK Cys343 to
353 form a disulfide linkage with $PorG_{Fj}$ (preferentially involving Cys225). In the absence
354 of either one of the $PorG_{Fj}$ cysteines formation of the disulfide bond with GldK relies
355 on adventitious oxidants and is inefficient.

356 We then examined the effects of altering the $PorG_{Fj}$ twin-cysteine motif on the
357 motions of fluorophore-tagged SprB adhesin molecules. Adhesins still moved in
358 continuous helical trajectories when $PorG_{Fj}$ lacked either one or both cysteine residues
359 (**Fig. 4g and Supplementary Video 3**) showing that adhesin movement on the tracks
360 does not require the disulfide link between $PorG_{Fj}$ and GldK. Thus, the gliding defects
361 in some of these mutants are most likely to be due to their reduced levels of adhesin
362 export (**Fig. 4c**, also evident by the larger proportion of rapidly diffusing non-exported
363 molecules in the periplasm of these strains in **Supplementary Video 3**) rather than
364 loss of adhesin function. An appreciable fraction of the adhesin trajectories in all three
365 *porG*$_{Fj}$ cysteine mutants showed mid-cell reversals rather than travelling fully to the
366 next pole. Examples are shown in **Fig. 4g and Supplementary Video 4**. This

367 behaviour is very rare in wild-type cells[17] suggesting that track morphology is
368 perturbed in the cysteine mutants and that $PorG_{Fj}$ may have a role in determining the
369 architecture of the gliding tracks.

370 As noted above, the $PorG_{Fj}$ cysteine motif is not rigidly conserved. For example,
371 the PorG protein of *P. gingivalis* is missing the cysteine residue that in *F. johnsoniae*
372 PorG forms the disulfide bond with GldK (**Fig. 4a**) raising the question as to whether
373 the remaining cysteine residue (Cys232) is required to support Type 9 function. We
374 found that removing this residue abolished Type 9 export in *P. gingivalis,* as judged by
375 the loss of colony pigmentation that is characteristic of T9SS-defective strains grown
376 on blood agar[39] (**Fig. 5a,b**). Thus, the single cysteine motif of *P. gingivalis* PorG is still
377 an essential requirement for Type 9 protein secretion. Generalising this observation
378 implies that all PorG C-tail cysteine motifs are involved in PorG function but that there
379 is flexibility in the exact complement and arrangement of the cysteine residues.

380

381 **Structure of the *P. gingivalis* PorKN Hub Complex**

382 We sought to understand the structural context of the disulfide link between
383 GldK/PorK and their partner OM proteins. Since we and others[15] have been
384 unsuccessful in isolating GldK-containing polymers from *F. johnsoniae* we
385 concentrated our efforts on the *P. gingivalis* PorKN complex which has previously been
386 characterized at low (>40 Å) resolution by cryo-EM and shown to form a large ring-
387 shaped structure[29]. We were able to improve the structure of the ~3 MDa PorKN ring
388 to near-atomic resolution (2.4 Å) (**Fig. 5c**, **Extended Data Figs. 6 and 7a**, **SI Table**
389 **1**). The PorK subunit is structurally defined from Gly32 to Phe476 and thus missing
390 the 8 N-terminal residues and 15 C-terminal residues of the mature protein. PorN is

391 defined from Thr47 to Trp299 and so is missing the 22 N-terminal residues and 62 C-
392 terminal residues of the mature protein (**Fig. 5d**). Two glycosylation sites are present
393 on each subunit, providing glycosylation on both the outer (PorK-linked) and inner
394 (PorN-linked) faces of the ring (**Fig. 5d**).

395 The PorKN ring is composed of multiple side-by-side PorKN heterodimer units (**Fig.**
396 **5c**), consistent with earlier biochemical evidence for an equimolar PorK:PorN
397 stoichiometry[29]. The actual number of repeats is not fixed, ranging from 31 to 35 PorKN
398 heterodimers, but is most frequently 33 (**Fig. 5c**), in agreement with the earlier lower-
399 resolution study of the complex which reported 32 to 36 repeating units[29]. Such
400 variation in subunit stoichiometry is commonly observed for ring complexes made up
401 from large numbers of repeating subunits[40,41], reflecting the small differences in
402 stability of oligomers of closely similar size.

403 The overall shape of the PorKN complex is consistent with earlier lower resolution
404 cryoEM and *in situ* cryoET studies of the complex [29-31], and our high resolution
405 structure is readily fit into the published lower-resolution envelopes for the complex
406 (**Fig. 5e**). The wall of the ring is angled inwards and is almost triangular in cross-
407 section, with the outer face more sloped than the inner (**Fig. 5f**). The 33-mer ring has
408 an outer diameter of 540 Å and an inner diameter of 380 Å (**Fig. 5c**). Published cryoET
409 images (and the fit of our model to these data, **Fig. 5e**) suggest that the face of the
410 ring formed by the base of the triangle is positioned next to the OM[30,31]. Consistent
411 with this assignment, the detergent micelle in our structure lies above this face of the
412 ring and is appropriately positioned to interact with the lipidated N-termini of the PorK
413 subunits (**Fig. 5c**). This membrane-facing side of the ring is noticeably flat (**Fig. 5c**)
414 and not highly charged, as would be appropriate for a surface that moves across the
415 face of the membrane. PorK and PorN form distinct layers of the ring (**Fig. 5c**), as

416 previously speculated[29]. The positions of the PorN subunits are somewhat offset
417 relative to PorK, resulting in each PorN subunit contacting two PorK subunits and vice
418 versa. The contacts between all neighbouring subunits are tightly packed and very
419 extensive, with the interactions between the well-folded subunit cores augmented by
420 a long N-terminal arm extended by each PorK subunit across the clockwise-adjacent
421 (as viewed from the OM) PorK molecule and shorter arms at the termini of the PorN
422 subunits which contact adjacent PorK molecules (**Fig. 5g**). These extensive contacts
423 bury more than ~5,500 $Å^2$ of surface for every PorKN pair incorporated into the ring
424 (**Fig. 5h**). This large interaction interface indicates a very stable complex in which the
425 subunit interactions are rigidly fixed. Likewise, the bulk of the individual subunits are
426 compactly folded implying they are rigid structures and there are no indications of
427 conformational flexibility anywhere within the ring in the cryoEM data. These
428 observations are difficult to reconcile with earlier interpretations of cryoET data as
429 showing a 40° variation in PorKN angle driven by the PorLM motors[30].

430 The core of the PorK subunit has an extensively elaborated sulfatase-modifying
431 enzyme (SME) fold[42], as previously noted[26], and contains the canonical disulfide bond
432 and bound metal atom (that we identify as a calcium ion based on the observed co-
433 ordination, **Extended Data Fig. 7b**) [42] that likely structurally stabilize the fold. The
434 extensions to the SME core found in PorK are involved in extensive interactions with
435 neighboring subunits, adding to the stability of the ring (**Fig. 5g**).

436 The PorN subunits have a well-folded core as seen in an earlier crystal structure of
437 this part of the subunit (RMSD 0.7 Å across 169 residues)[43]. However, both the N and
438 C-termini become ordered in assembling the ring, with the N-terminus packing against
439 PorK and the C-terminus packing on the inner face of the PorN portion of the ring (**Fig.
440 5f,g**). Unsurprisingly, the residues buried in assembling the ring are conserved.

441 The PorG-reactive cysteine residue Cys356 is exposed on the OM-facing side of
442 PorK, congruent with its role in interacting with the OM-embedded PorG, and is located
443 at the inner rim of the PorKN ring (**Fig. 5g,i**). Cys356 is found in a conserved Arg-Gly-
444 Cys-Phe motif (**Fig. 3a**) with the arginine presented at the apex of a small surface loop
445 that projects away from the protein core and is stabilized by intra-loop backbone
446 hydrogen bonds. Within this loop the side chain of Arg354 sits above Cys356 partially
447 screening it from interacting partners (**Fig. 5i**) although the cysteine side chain remains
448 highly solvent exposed.

449 We used AF3 to model the interaction between PorG and PorKN. AF3 recapitulated
450 the structure of PorKN well (RMSD 2.8 Å overall for a 3:3 heterocomplex, **Extended**
451 **Data Fig. 7c**) and demonstrated that interactions between PorG and the ring are likely
452 limited to the linking disulfide bond and interactions from residues immediately
453 surrounding the disulfide in the unstructured tail of PorG (**Extended Data Fig. 7d**). In
454 particular, no consistent or high confidence interactions were predicted between the
455 base of the PorG barrel and the upper surface of the ring. We also used AF3 to predict
456 interactions between the PorM dimer arm of the PorLM motor that energizes the
457 PorKN ring (**Extended Data Fig. 7e**). The tip of the PorM dimer is predicted to lie
458 within the cleft formed between neighbouring copies of PorN at the periplasmic face
459 of the ring, with the majority of the contacts coming from one copy of the D4 domain
460 of PorM. The surface buried in this interaction is not substantially conserved or
461 charged and the confidence metrics also give little support for this mode of interaction.
462 Previous biochemical and genetic interaction data had suggested that PorM interacts
463 with both PorN and PorK[43-45] but only PorN contacts are supported by this modelling.

464

465 **Model for the *F. johnsoniae* gliding track structure**

466 In this work we have discovered that the adhesin carrier protein SprF is covalently
467 attached to the OM lipoprotein GldK through a disulfide bond. Since SprF is known to
468 be propelled around the cell by interactions with the gliding tracks this implies that
469 GldK is a component of the gliding track. This conclusion contrasts with the current
470 model for the gliding machinery where GldK is part of a PorKN-like Hub complex that
471 is distinct from the gliding track itself (**Fig. 1a**).

472 We probed the structural plausibility of our new model for the organisation of the
473 gliding track by using AF3 to predict the structure formed by the *F. johnsoniae* GldKN
474 oligomer and how this interacts with the only currently known gliding track component
475 GldJ. Predictions containing equal numbers of GldK, GldN, and GldJ protomers
476 formed a high confidence and well-packed filamentous structure (**Fig. 6a**). Within this
477 filament the GldKN subunits have essentially the same arrangement as the equivalent
478 subunits in the *P. gingivalis* PorKN structure (231 core residue superimpose with an
479 RMSD of 0.7A).The GldJ subunits, which are structurally related to GldK[21,32], mimic
480 the organisation and placement of the GldK protomers but are on the opposite side of
481 the filament and run in the reverse direction along the filament. The result is that GldK
482 and GldJ pack alongside each other in two antiparallel lines on the OM-proximal side
483 of the filament with both subunits in contact with GldN. The packing between all three
484 types of subunits is extensive and indicative of a single stable entity consistent with
485 the idea that the filament represents the gliding track and that GldK and GldN are
486 components of the track. In our model the SprF/PorG-interacting Cys343 of GldK is
487 positioned at the centre of the OM-facing surface of the filament at the interface
488 between the lines of GldJ and GldK subunits. (**Fig. 6a**) We note that our model for the

489 interactions between GldJ and GldK differs from a recent proposal based on
490 computational docking[23].

491

492 ## Discussion

493 In *F. johnsoniae* the carrier protein SprF spans the OM to link the major cell surface
494 gliding adhesin SprB to the internal gliding track. In this work we have discovered that
495 SprF forms a disulfide bond at the periplasmic face of the OM with the protein GldK.
496 At steady state almost all the SprF molecules in the cell have this disulfide linkage
497 (**Figs. 2a,b and 3c**). Because almost all the SprF molecules are also carrying
498 adhesins along the gliding tracks (**Figs. 1e,3e, and 4g and Supplementary Video 1**),
499 it can be inferred that the disulfide link must be to a track component and, thus, that
500 GldK is part of the gliding track. This conclusion overturns the current model of the
501 gliding apparatus in which GldK is considered to be a component of a Hub complex
502 that links the gliding motors to the gliding tracks[13,22,23] (**Fig. 1a**). Instead, it suggests
503 that GldK and its Hub partner GldN are integral components of the gliding track (**Fig.
504 6c**), a possibility that has been briefly considered by some authors[3]. Several lines of
505 evidence support the new model for the organisation of the gliding track. First, AF3
506 modelling predicts a high-confidence equimolar complex between the Hub proteins
507 GldK and GldN and the known track protein GldJ. The resulting complex is stabilised
508 by extensive tight packing between all three of the constituent protomer types, and the
509 proteins are arranged in a repeating filament-like structure as expected of the track
510 (**Fig. 6a**). The possibility that the predicted interactions instead represent an interfacial
511 contact between the moving Hub and track complexes is unlikely, not only because of
512 the very tight predicted packing but because the GldJ 'track' should contact the outside

513 of the ring in a sprocket-and-chain model whilst the structure prediction locates it on
514 the equivalent of the inner face of the PorKN ring (**Fig. 6a**). Second, the previously
515 observed stabilisation of GldK by GldJ[46] is better interpreted in terms of GldK forming
516 part of a GldJ-containing gliding track than GldK being part of a separate Hub complex
517 that does not contain GldJ. Third, a SprF variant (Cys324Ala) that we infer cannot
518 easily reverse its attachment to GldK is still able to move helically for multiple circuits
519 of the cell implying that it must be attached to GldK throughout those circuits (**Figs.**
520 **1e, 2a and Supplementary Video 1**). Finally, the fact that only SprF molecules that
521 can form a disulfide link with GldK are able to mediate continuous helical movement
522 of adhesins along the tracks (**Figs. 1e and 3e and Supplementary Video 1**) is also
523 consistent with GldK being part of the track.

524 SprF is still able to interact transiently with the gliding track in the absence of the
525 disulfide linkage to GldK (**Figs. 1e and 3e and Supplementary Video 1**), indicating
526 that there are disulfide-independent interactions between SprF and the track but that
527 these are weaker than those mediated by the disulfide bond. These weak interactions
528 may be required for initial complex formation between SprF and GldK to allow
529 subsequent disulfide bond creation. We envisage that the disulfide bond provides a
530 very stable linkage between the track and SprF that allows the track to exert force on
531 those adhesin molecules that are bound to the external substratum in order to propel
532 the cell forward (high load). Even under the low load conditions used in our
533 experiments, where the cells are suspended in agarose rather than pushing against a
534 surface, the very long (~200nm[15]) SprB adhesins may still require substantial force to
535 move them through the medium surrounding the cell and, thus, still show strong
536 dependence on the presence of the SprF-GldK disulfide linkage.

537 Remarkably, we found that SprF is not the only OM protein bound to GldK. The
538 T9SS component PorG makes an equivalent linkage to GldK, and this is important for
539 Type 9 protein transport. Although SprF and PorG bind to the same cysteine residue
540 in GldK, it is unlikely that their binding is competitive because GldK is in large molar
541 excess over either protein (**Fig. 2a and Extended Data Fig. 4**). The presence of a
542 disulfide linkage between PorG and GldK allows us to predict that PorG moves on the
543 gliding track like SprF. We also deduce that this movement results in the exertion of
544 considerable mechanical force, necessitating the covalent attachment of PorG to the
545 track. Because the ejection of carrier protein-substrate complexes from the T9SS
546 translocon is the energy-requiring step in Type 9 transport[8] we speculate that the role
547 of PorG might be to transmit force from the Energy Chain to push carrier proteins out
548 of the translocon. Intriguingly, we find that cells that fail to make a disulfide connection
549 between PorG and GldK show apparent alterations in long-range track morphology
550 (**Fig. 4g**) suggesting that PorG has a role in track placement, perhaps by displacing
551 other OM proteins from the track path. We find that full deletion of the PorG protein
552 has a stronger effect on export of the Type B T9SS substrate SprB than achieved by
553 blocking disulfide bond formation between PorG and GldK (**Fig. 4c,g**). This indicates
554 that, like SprF, PorG possesses disulfide-independent interactions, potentially with the
555 gliding track.

556 One major takeaway from the structure of the *P. gingivalis* PorKN Hub complex is
557 that is has no substantive conformational flexibility. This suggests that force exerted
558 on the Hub by the motor complexes cause it to rotate in place as a rigid body carrying
559 any attached partner proteins with it (**Fig. 6b**). Our modelling data suggest that the
560 motor complexes push on the OM-distal end of the PorN subunit (**Extended Fig. 7e**).
561 The energetic barrier to rotation of the PorKN ring is minimised because it is anchored

562 to the OM only by lipid tails on the PorK subunits and sub-stoichiometric quantities of
563 the integral membrane PorG protein. The GldJKN filaments would move linearly in a
564 very similar manner to the PorKN ring, with the GldN subunits providing closely spaced
565 contacts all along the filament for the gliding motors to push on (**Fig. 6b**).

566 An interesting question is why both *F. johnsoniae* SprF and $PorG_{Fj}$ require two
567 cysteine residues to realise their physiological disulfide linkage to GldK. Two, not
568 mutually exclusive, possibilities can be considered. First, that the periplasmic thiol-
569 oxidizing proteins required for disulfide bond formation cannot access the SprF/$PorG_{Fj}$-
570 GldK interface and so a progenitor disulfide bonds must be introduced into SprF and
571 $PorG_{Fj}$ during biogenesis that are then attacked by the GldK cysteine (**Fig. 3f**). This
572 suggestion is supported by the AF3 model of the gliding track which shows that the
573 GldK cysteine is located in the centre of the side facing the OM and is, therefore,
574 relatively inaccessible (**Fig. 6a**). Second, the presence of the second cysteine could
575 allow the link with GldK to be reversibly broken (**Fig. 3f**), for example to allow SprF or
576 $PorG_{Fj}$ to move between tracks or temporarily detach at track crossings. However, this
577 cannot be an essential requirement during regular adhesin movement as a single
578 cysteine SprF variant (Cys324Ala) that should be locked onto the track is still able to
579 make multiple passages up and down the cell (**Figs. 1e, 2a, and Supplementary**
580 **Video 1**). Intriguingly *P. gingivalis* PorG only has a single cysteine rather than the two
581 cysteines seen in the *F. johnsoniae* PorG protein. This would be consistent with either
582 of the two scenarios just outlined. First, the PorKN ring the PorG-reactive cysteine is
583 exposed on the inner edge of the ring rather than being sequestered within the ring-
584 OM interface (**Fig. 5b**) and so would in this case be easily accessible to thiol oxidising
585 proteins. Second, the PorKN rings act in isolation from each other[30,31] and so there is
586 no requirement for $PorG_{Pg}$ to move between rings. Although these are explanations

587 provide attractive rationales for the different numbers of cysteines found in *F.*
588 *johnsoniae* and *P. gingivalis* PorG it is worth noting that there is no simple correlation
589 between the number of cysteines present in the PorG periplasmic tail and whether an
590 organism is a gliding or non-gliding bacterium (**Fig. 4a**).

591 Our new model of the organisation of the gliding track indicates its likely
592 evolutionary relationship with the T9SS. We suggest that the T9SS first evolved as a
593 component of the Bacteroidota gliding machinery in order to place gliding adhesins on
594 the cell surface (**Fig. 6c**). This would explain why Type 9 transport uses a very unusual
595 mechanism in which protein export involves forming a complex with an OM carrier
596 protein rather than the substrate being directly exported. This is an ideal strategy for
597 adhesin export because the adhesin needs to end up anchored to an OM adaptor
598 protein that connects it to the gliding track. The gliding track would also be conveniently
599 positioned to accept the adhesin-carrier protein complex from the translocon because
600 it is already involved in energizing the translocon. In non-gliding bacteria, such as *P.*
601 *gingivalis,* the gliding function of the track is no longer required. However, the track is
602 still required to power Type 9 export. We, envisage that in these bacteria the track has
603 become miniaturised as the PorKN ring and retained solely to provide energy to the
604 translocon (**Fig. 6b**). The suggested evolutionary relationship between gliding motility
605 and Type 9 protein transport has parallels with the relationship between the
606 nanomachines constituting the bacterial flagellum (a motility system that exports its
607 own components) and Type 3 Secretion Systems (secretion only)[47].

Acknowledgments

We thank James Horne for producing the PorN and GldJ antisera and *F. johnsoniae* Δ*gldK* and Δ*porG* mutants, Mark McBride for providing SprF and GldK antisera, Frederick Lauber for producing the Δ*sprF* mutant, Kevin Foster for access to anaerobic culture and imaging facilities, and James Garnett, Mark Roberts, Joseph Aduse-Opoku, Michael Curtis, and Graham Stafford for strains, reagents, and advice on working with *P. gingivalis*. We acknowledge the use of Oxford Micron Advanced Imaging Facility. This work was supported by European Research Council Advanced Award 833713 (BCB), Biotechnology and Biological Sciences Research Council grant BB/S007474/1 (BCB and SML), and a Medical Research Council studentship to RJ. This research was supported in part by the Intramural Research Program of the NIH.

Author Contributions

XL carried out all genetic and biochemical experiments, with the exception that MA purified the PorKN complex. JCD, CL, and SML collected electron microscopy data and determined all structures. RJ and XL carried out fluorescence microscopy experiments. XL, BCB, and SML conceived the project. BCB and SML secured funding. The draft manuscript was written by XL and BCB. All authors interpreted data, produced figures, and revised the manuscript.

Competing interests

The authors declare no competing interests.

631 # Methods

632 ## Bacterial strains and growth conditions

633 All strains used in this work are listed in Supplementary Table 2.

634 *F. johnsoniae* was routinely grown aerobically in Casitone Yeast Extract (CYE)
635 medium[48] at 30 °C with shaking. For some physiological studies the cells were cultured
636 in Motility Medium (MM)[49] or PY2 medium[50].

637 *P. gingivalis* was grown anaerobically (5 % CO_2, 5 % H_2, 90 % N_2) at 37 °C in a Don
638 Whitley Scientific A45 workstation. For liquid culture *P. gingivalis* was grown in brain
639 heart infusion (BHI) medium (Oxoid) supplemented with 5 µg/ml haemin, 1 µg/ml
640 menadione, 0.5 mg/ml L-cysteine (BHIS). Culture on blood agar (BA) plates (blood
641 agar base (Oxoid), 50 µl/ml defibrinated horse blood (HB034, TCS Biosciences Ltd),
642 5 µg/ml haemin, 1 µg/ml menadione, 0.5 mg/ml L-cysteine) was used to obtain single
643 colonies. Where required, antibiotics were used at the following concentrations: 30
644 µg/ml erythromycin, 1 µg/ml tetracycline, 3 µg/ml carbenicillin (in BHIS liquid medium),
645 and 40 µg/ml carbenicillin (on BA solid medium).

646

647 ## Genetic constructs

648 Plasmids were constructed by Gibson assembly[51] or Q5 site-directed mutagenesis
649 (New England Biolabs) using the primers and target DNA in Supplementary Tables 3
650 and 4. All *F. johnsoniae* and *P. gingivalis* mutations were constructed in the native
651 chromosomal genes.

652 Chromosomal modifications were introduced into *F. johnsoniae* using the suicide
653 vector pYT313[52] harbouring the counter-selectable *sacB* gene as previously

654 described[25]. Suicide and expression plasmids were introduced into the appropriate *F.*
655 *johnsoniae* background strain by triparental mating using DH5α transformed with the
656 plasmid to be transferred and HP101 containing the helper plasmid pRK2013 as
657 previously described[48].

658 Linear DNA fragments were used for chromosomal modification in *P. gingivalis* and
659 introduced by electroporation. Electrocompetent cells were prepared from *P. gingivalis*
660 grown anaerobically to OD_{600} = 0.7. From this point manipulations were carried out
661 outside the glove box until anaerobic conditions were re-established after
662 electroporation. The cultures harvested by centrifugation at 10,000*g* for 10 min at 4°C,
663 then resuspended in ice-cold electroporation buffer (10% glycerol, 1 mM $MgCl_2$) and
664 pelleted again under the same conditions. This washing step was repeated once more
665 before resuspending the final electrocompetent cells in 200 µl of electroporation buffer.
666 Electroporation was performed by mixing the electrocompetent cells with 0.5–2 µg of
667 transforming DNA in an 2 mm electroporation cuvette (165-2086, Bio-Rad) and pulsing
668 at 2500 V for 5 ms in a BTX ECM 399 Electroporation System (SLS). Following
669 electroporation, the cuvette was returned to the glove box, supplemented with 1 ml
670 deoxygenated BHIS medium, and incubated for 24 h to allow the cells to recover. If
671 *cepA* was used as the selective marker the cultures were then diluted 1:100 in BHIS
672 supplemented with 3 µg/mL carbenicillin and incubated until turbid (5–7 days). A
673 dilution series was then plated on blood agar plates supplemented with 40 µg/mL
674 carbenicillin. For other selection markers the transformed culture was plated directly
675 onto BA supplemented with the appropriate antibiotic.

676 To facilitate genetic modification of *P. gingivalis* in a triple gingipain deleted
677 background the *rgpB*::*ermAM-F* locus in strain EK18[53] was replaced with *cepA* using
678 a SmaI-digested fragment of pCL54 to produced strain P54.

679 All plasmid constructs and chromosomal modifications were confirmed by
680 sequencing.
681

682 **Immunoblotting and antisera used.**

683 Immunoblotting was carried out as previously described[8]. Polyclonal antibodies
684 against GldJ and PorN were raised in rabbits against synthetic peptides. Polyclonal
685 antibodies against SprF[11], GldK[26], and SprA[54] were provided by Mark McBride
686 (University of Wisconsin-Milwaukee). The following commercial antisera were used:
687 anti-HaloTag (G921A, Promega), anti-GroEL (G6532 Merck), anti-mCherry
688 (ab167453, Abcam), anti-ALFA-Tag (N1582, Synaptic Systems GmbH), anti-mouse
689 IgG peroxidase conjugate (A4416 Merck), and anti-rabbit IgG peroxidase conjugate
690 (31462 Pierce).
691

692 **Analytical methods**

693 The protease protection assay for SprB export and the analysis of mCherry-CTD
694 secretion were carried out as previously described[8].

695 Measurements of gliding motility on agar and analysis of the secreted proteome
696 were performed as previously described[7].

697

698 **Whole cell analysis of disulfide-bonded protein complexes**

699 The *F. johnsoniae* strain to be analyzed was grown overnight in 5 ml CYE medium,
700 diluted 1:100 into 15 ml fresh CYE medium, and cultured until OD_{600}=0.6. Cells were
701 collected by centrifugation at 8,000*g* for 5 min, washed in PBS buffer, and

702 resuspended in PBS buffer to OD_{600}=1. The sample was aliquoted equally into two
703 0.5ml fractions which were then either supplemented or not with 5 mM *N*-
704 ethylmaleimide (E3876-5G, Merck) and incubated for 5 min in the dark on a roller at
705 room temperature. Each sample was aliquoted equally into two 0.25 ml fractions that
706 were then pelleted, washed in PBS, resuspended in PBS, and boiled for 5 min with 1x
707 SDS-PAGE sample buffer either with or without 100 mM DTT, then analyzed by
708 immunoblotting. For the protonophore treatment experiments the growing culture was
709 supplemented with 10 μM CCCP (C2759-1G, Merck) for 20 min before harvesting the
710 cells, and 10 μM CCCP was then maintained throughout the sample preparation
711 procedure.

712

713 **Live cell fluorescence microscopy**

714 *F. johnsoniae* strains were cultured in MM to OD_{600} = 0.4 and 900 μl added to an
715 Eppendorf tube containing 100 μl of MM pre-mixed with 1 μl of a 10 nM solution of
716 Janelia Fluor JFX650 HaloTag Ligand (Promega) in dimethyl sulfoxide. The tubes
717 were shaken at 30 °C for 20 min and the cells then pelleted by centrifugation at
718 7,000*g* for 3 min. The cells were washed four times by resuspension in 1 ml of PY2
719 medium and repelleting, and finally resuspended in 200 μl PY2 medium. 1 μl of this
720 cell suspension was spotted onto agarose pads formed from 1% agarose in PY2
721 medium and then imaged.

722 All imaging data were acquired on a Nanoimager (Oxford Nanoimaging) equipped
723 with a 640 nm 1W DPSS laser. Optical magnification was provided by a 100× oil-
724 immersion objective (Olympus, numerical aperture (NA) 1.4) and images were
725 acquired using an ORCA-Flash4.0 V3 CMOS camera (Hamamatsu). All fluorescence

726 images were collected at 15% laser power using 30 ms continuous exposure. Where
727 applicable, data were acquired in 3D by engaging the astigmatic lens of the
728 Nanoimager. The z-co-ordinate was calibrated by taking a z-stack in 2 nm increments
729 in the range -1 μm to +1 μm from focus, of 0.1 μm tetraspec beads (T7279, Invitrogen)
730 immobilised on a glass slide with poly-L-lysine.

731 Raw data were analysed using the Fiji plugin ThunderSTORM[55] to determine single
732 molecule localisations. Single molecule trajectories within cells were computed using
733 a custom Python script that incorporated the Trackpy package
734 (https://doi.org/10.5281/zenodo.1213240), with a memory allowance of 2 frames and
735 a search range of 3 pixels per frame. Tracks were filtered using a minimum length of
736 30 frames.

737

738 **Purification of PorKN complexes**

739 PorKN complexes were purified by modifying a previously described method[29,56].
740 The complexes were purified from a triple gingipain-deleted mutant of *P. gingivalis*
741 W50 (EK18). In this *P. gingivalis* strain PorK is PG_0288 and PorN is PG_0291. The
742 strain was grown under anaerobic conditions in 10 l of BHIS broth to an OD_{650} of 1.
743 Cells were harvested by centrifugation at 15,000*g* for 1 h. The pellet was resuspended
744 in lysis buffer (50 mM TrisHCl pH 7.5, 150 mM NaCl, 0.5 M sucrose, 5 mM $MgCl_2$, 1%
745 (w/v) n-Dodecyl β-D-maltoside (DDM)(Anatrace), benzonase (Sigma-Aldrich) and
746 cOmplete™ Protease Inhibitor Cocktail (Sigma-Aldrich)) and gently mixed using a
747 magnetic stirrer at 4 °C for 3 h. The resulting lysate was clarified by centrifugation at
748 10,000*g* at 4 °C for 1 h. Na_2EDTA was added to the clarified supernatant to a final
749 concentration of 10 mM, and then lysozyme powder (Sigma-Aldrich) was added to a

750 final concentration of 0.5 mg/ml. The mixture was then incubated at 37 °C for 45 min
751 followed by centrifugation at 210,000*g* at 4 °C for 90 min. The resulting pellet was
752 resuspended in resuspension buffer (10 mM Tris HCl pH 7.5, 500 mM NaCl, 5 mM
753 Na_2EDTA, 1% (w/v) DDM) and centrifuged at 10,000*g* at 4 °C for 15 min to remove
754 unsolubilised material. The recovered supernatant was mixed at a ratio of 1:3 with a
755 30% CsCl solution (30% (w/v) CsCl, 10 mM Tris HCl pH 7.5, 0.5% (w/v) DDM] and
756 then centrifuged at 215,000*g* at 20 °C for 19 h in a SW55 Ti rotor (Beckman-Coulter).
757 Fractions were sampled from the top downwards with a wide-bore pipette tip. 10
758 soluble fractions were isolated, followed by a loose pellet (LP) fraction containing the
759 soluble PorKN complexes, and an insoluble pellet (P) fraction. Fractions were diluted
760 at a ratio of 1:2 with dilution buffer (10 mM Tris HCl pH 7.5, 500 mM NaCl, 0.5% (w/v)
761 DDM, 5 mM Na_2EDTA) and the PorKN complexes pelleted by centrifugation at
762 210,000*g* for 2 h. The pellets were resuspended in sample buffer (10 mM Tris HCl pH
763 7.5, 500 mM NaCl, 0.5% (w/v) DDM) and successful fractionation confirmed by
764 immunoblotting using a PorN antibody. The LP fraction (400 µL) was loaded onto a
765 discontinuous sucrose gradient formed by layering equal volumes (400 µL) of,
766 successively, 2 M, 1.9 M, 1.8 M, 1.7 M, 1.6 M, 1.5 M, and 1 M sucrose in dilution buffer.
767 The gradients were centrifuged at 215,000*g* at 12 °C for 17 h in a SW55 Ti rotor
768 (Beckman-Coulter). Fractions were sampled from the top downwards with a wide-bore
769 pipette tip, 11 fractions were isolated (F1 to F11, with F1 being the upper-most
770 fraction). Fractions were diluted at a ratio of 1:2 with dilution buffer and the PorKN
771 complexes pelleted by centrifugation at 250,000*g* for 1 h 45 min. The pellets were
772 resuspended in sample buffer and then analysed by SDS-PAGE and by
773 immunoblotting using a PorN antibody to identify the fractions (typically F6 and F7)
774 containing the highest concentration of PorKN rings. These fractions were pooled and

775 pelleted at 186,000*g* for 2 h at 12 °C. The pellet was resuspended in 30 µl sample
776 buffer and used to prepare cryoEM grids.

777

778 **Cryo-EM sample preparation and imaging**

779 3 µl of the PorKN sample (A_{280nm} = 7.2) was applied to ultra-thin carbon coated
780 grids (Quantifoil 300 mesh, Au R2/1) at 4°C in 100% humidity. The sample was
781 adsorbed for 60 s, blotted 3 s, and plunge frozen in liquid ethane using a Vitrobot mark
782 IV (FEI).

783 Movies were collected in counted mode, in Electron Event Representation (EER)
784 format, on a CFEG-equipped Titan Krios G4 (Thermo Fisher Scientific) operating at
785 300 kV with a Selectris X imaging filter (Thermo Fisher Scientific) and slit width of 10
786 eV, at 165,000x magnification on a Falcon 4i direct detection camera (Thermo Fisher
787 Scientific), corresponding to a calibrated pixel size of 0.732 Å. Movies were collected
788 at a total dose of 55.0 (Table 1), fractionated to ~ 1.0 $e^{-}/Å^2$ per fraction for motion
789 correction.

790

791 **Cryo-EM data processing**

792 Patched motion correction, CTF parameter estimation, particle picking, extraction,
793 and initial 2D classification was performed in SIMPLE 3.0[57]. All downstream
794 processing was carried out in cryoSPARC[58]. Global resolution was estimated from
795 gold-standard Fourier shell correlations (FSCs) using the 0.143 criterion and local
796 resolution estimation was calculated using the 0.5 criterion.

797 The cryo-EM processing workflow for PorKN is outlined in **Extended Data Fig. 6**.
798 Briefly, particles were downsampled from 0.732 Å/pixel to 1.464 Å/pixel and subjected
799 to one round of reference-free 2D classification (k=100) using a 600 Å soft circular
800 mask. Selected particles (162,414) were further downsampled to a pixel size of 2.928
801 Å and subjected to another round of 2D classification (50 classes, no mask), yielding
802 124,099 cleaner particles. A low resolution volume was generated from these particles
803 after *ab initio* reconstruction with D33 symmetry applied. Corresponding particles were
804 then non-uniform refined (applying D33 symmetry, 10 Å lowpass filter) against this
805 volume, resulting in a Nyquist-limited 5.9 Å volume. Unmasked 3D classification of the
806 particles was then performed against 10 classes using a resolution filter of 8 Å while
807 applying D33 symmetry. Particles belonging to the most symmetric and structured
808 volume were re-extracted to a pixel size of 1.7568 Å/pixel after re-centring using prior
809 aligned shifts. This was followed by non-uniform refinement (D33 symmetry) against
810 a corresponding 10 Å lowpass-filtered volume that generated an improved 4.0 Å
811 volume. Local refinement using a rotational search extent of 5 degrees and shift extent
812 of 3 Å was performed on D33 symmetry-expanded particles (1,097,778) in C1 against
813 the corresponding map lowpass-filtered to 8 Å, using a soft mask covering multiple
814 subunit copies on the ring, resulting in a 3.5 Å Nyquist-limited reconstruction. Particles
815 and corresponding volume were then re-centred to the mask centre of mass and re-
816 extracted using these aligned shifts to a pixel size of 1.1764 Å/pixel. These particles
817 were subjected to local refinement using limited searches (5° angular, 3 Å shifts),
818 resulting in a 3.1 Å volume. Local CTF refinement followed by an identical local
819 refinement scheme further improved map quality to 2.5 Å. Particles were then re-
820 extracted using their aligned shifts to a pixel size of 1.097 Å, followed by an additional
821 round of C1 local refinement that generated a slightly improved 2.5 Å volume. Focused

822 3D classification using a mask covering three subunits on the ring was performed
823 against 4 classes in C1 and using a resolution filter of 3 Å. Particles belonging to the
824 most populated class were selected and underwent local refinement (C1), generating
825 a 2.4 Å volume from 676,608 particles.

826

827 **Model building, structure refinement, and figure preparation**

828 Iterative model building and real-space refinement using rotamer, and
829 Ramachandran restraints was performed in Coot v0.9[59] and Phenix[60], respectively.
830 Validation was performed in Molprobity[61] within Phenix. Cryo-EM data collection,
831 image processing and structure refinement statistics are listed in Supplementary Table
832 1. Figures were prepared using UCSF ChimeraX v.1.9[62].

833

834 **Statistics and reproducibility**

835 All experiments shown in the paper are representative with similar data obtained for
836 at least three biological repeats.

837

838 **Data availability**

839 Cryo-EM density maps and atomic coordinates are deposited in the Electron
840 Microscopy DataBank (EMDB) with the following accession number: EMD-48769.
841 Atomic coordinates are deposited in the Protein Data Bank (PDB) with the following
842 accession number: PDB 9MZU.

843 Gel and immunoblot source data are published alongside this paper.

https://github.com/notdrjones/Single-Particle-Tracking-for-Disulfide-Bond-Paper

Requests for materials should be addressed to BCB.

Code availability

Original code used in this study is available at https://github.com/notdrjones/Single-Particle-Tracking-for-Disulfide-Bond-Paper.

850 **Supplementary Video 1. Mobility of fluorophore-tagged SprB adhesin molecules**
851 **in *F. johnsoniae* cells with mutations in *sprF*.** Raw images were recorded with
852 continuous exposure at 33 fps using epifluorescence microscopy. Playback is in real
853 time. The area of the field of view is 32.7 x 32.7 μm.

854 **Supplementary Video 2. Mobility of fluorophore-tagged SprB adhesin molecules**
855 **in *F. johnsoniae* cells with mutations in *gldK*.** Raw images were recorded with
856 continuous exposure at 33 fps using epifluorescence microscopy. Playback is in real
857 time. The area of the field of view is 32.7 x 32.7 μm.

858 **Supplementary Video 3**. **Mobility of fluorophore-tagged SprB adhesin molecules**
859 **in *F. johnsoniae* cells with mutations in *porG*.** Raw images were recorded with
860 continuous exposure at 33 fps using epifluorescence microscopy. Playback is in real
861 time. The area of the field of view is 32.7 x 32.7 μm.

862 **Supplementary Video 4. Single particle tracking of a fluorophore-tagged SprB**
863 **adhesin molecule in a *F. johnsoniae porG*^{C225S,C227S} mutant cell showing mid-cell**
864 **reversals.** Raw images were recorded with continuous exposure at 33 fps using
865 epifluorescence microscopy. Overlaid on the image is the real time progression of the
866 super-resolution fit of the adhesin trajectory, coloured by time. The scale bar
867 represents 1 μm.

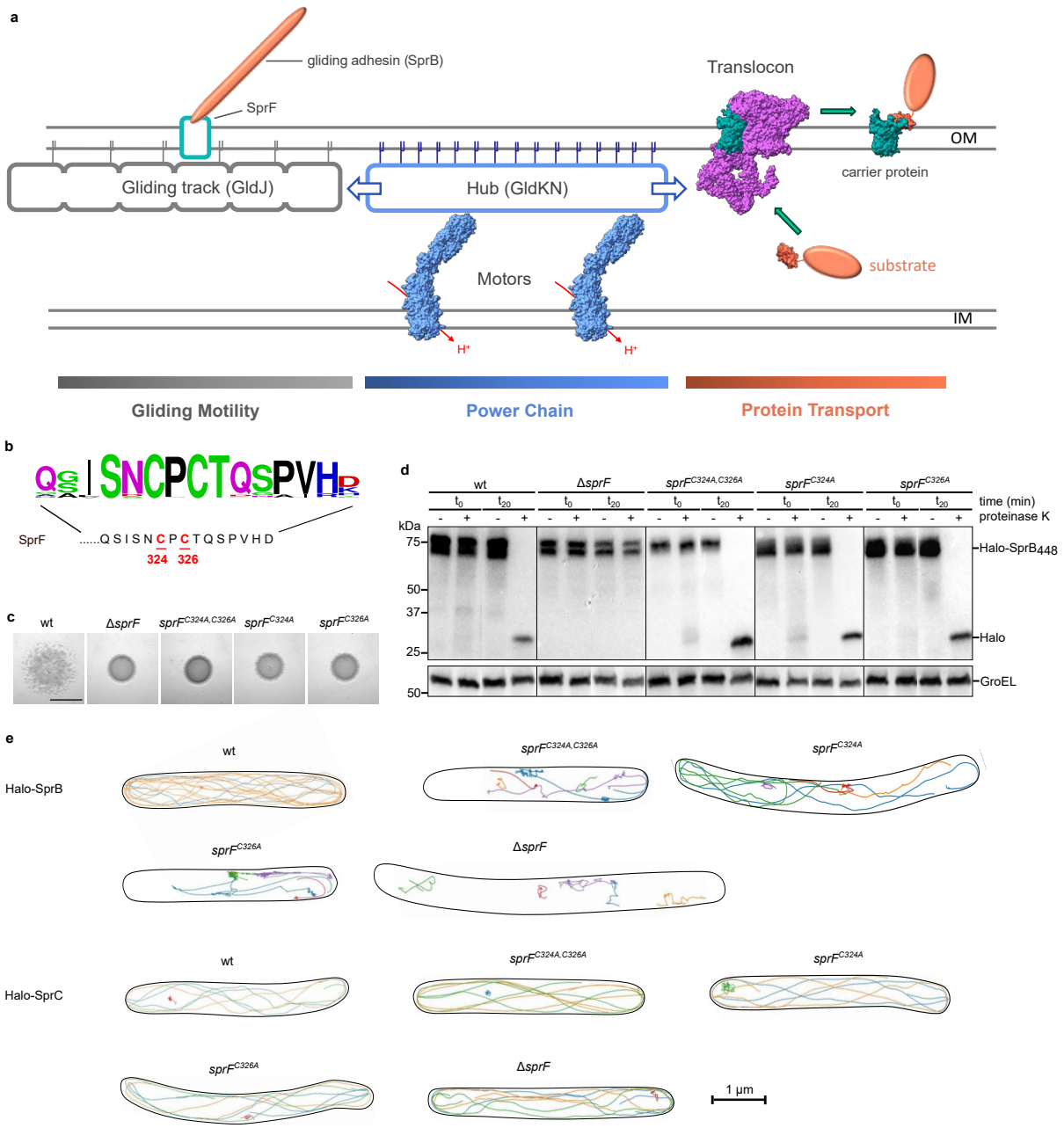

Fig. 1 | The cysteine residues in the periplasmic C-tail of SprF are essential for SprB movement and gliding motility.

a, Current model for the organization of the gliding motility apparatus and T9SS in *F. johnsoniae* involving a shared Power Train. OM, outer membrane. IM, inner membrane.

b, Sequence of the periplasmic C-tail of *F. johnsoniae* SprF with the twin-cysteine motif highlighted and a Weblogo display of the sequence conservation (500 closest whole protein homologues) above.

c-e, Characterization of *sprF* mutants with substitutions in the conserved cysteine pair. wt, wild type. Similar results were obtained for 3 biological repeats.

879 **c**, Spreading (gliding) morphology on agar. Scale bar, 5mm.
880 **d,** Cell surface exposure of the adhesin SprB assessed by protease protection. The indicated
881 strains expressing a fusion between HaloTag and the final 448 amino acids of SprB (Halo-
882 $SprB_{448}$) were incubated with Proteinase K (+ lanes). Reactions were stopped immediately (t_0)
883 or after 20 min (t_{20}) and analysed by immunoblotting with Halotag antibodies. The cytoplasmic
884 protein GroEL serves as a both a loading and cell integrity control. In each panel (which
885 correspond to separate immunoblots) a lane has been removed between the t_0 and t_{20}
886 samples.
887 **e**, Exemplar trajectories of single fluorophore-labelled HaloTag-SprB adhesin molecules or
888 HaloTag-SprC molecules in the indicated backgrounds. The trajectories link the single
889 molecule localizations in successive frames recorded for agarose-immobilised cells and are
890 2D projections of what is a 3D process. Each trajectory within a cell is shown in a different
891 colour and the segmented outline of the cell is shown in black. For the SprF cysteine variants
892 cells were chosen to illustrate the observed range of SprB mobility behaviours. See also
893 Supplementary Video 1.

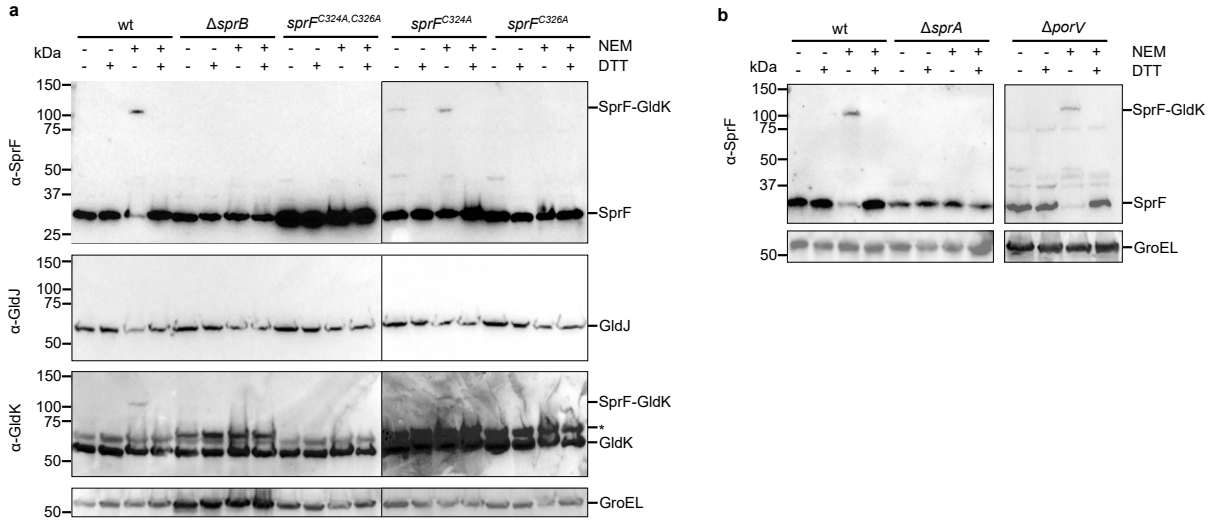

Fig. 2 | SprF forms a disulfide bond with the Hub protein GldK.

Strains with the indicated mutations were subject to whole cell immunoblotting with the specified antisera. Where indicated the cells were pre-treated with NEM. At the SDS-PAGE step samples were run under either non-reducing (- DTT) or reducing (+ DTT) conditions. GroEL serves as a loading control. *, non-specific background band. wt, wild type; a strain missing the T9SS translocon (Δ*sprA*); a strain missing the Type A carrier protein PorV (Δ*porV*). Similar results were obtained for three biological repeats.

a, SprF forms disulfide bonds with GldK but not GldJ.

b, Formation of a disulfide bond between SprF and GldK depends on Type 9 transport activity but is independent of Type A T9SS export.

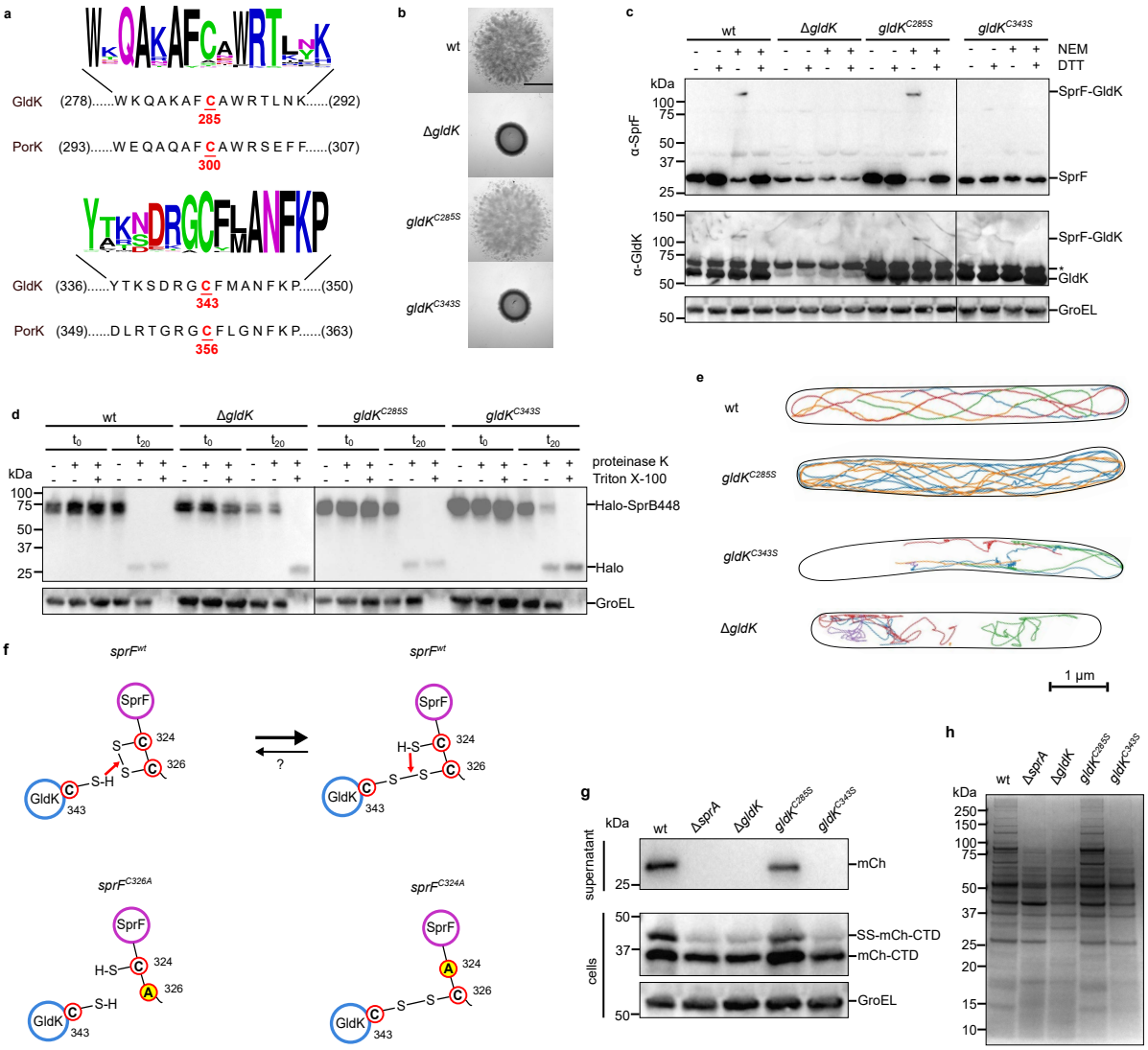

Fig. 3 | Identification and functional characterization of the SprF-crosslinking residue in GldK.

a, The sequences of the two cysteine-containing polypeptide regions of *F. johnsoniae* GldK and the corresponding regions of *P. gingivalis* PorK. Above is a Weblogo display of the sequence conservation for sequences with >40% whole protein identity to GldK.

b,c, Identification of the GldK cysteine that forms the disulfide linkage with SprF.

b, Spreading (gliding) morphology on agar. Scale bar, 5mm.

c, Strains with the indicated mutations were subject to whole cell immunoblotting with the specified antisera. Where indicated the cells were pre-treated with NEM. At the SDS-PAGE step samples were run under either non-reducing (- DTT) or reducing (+ DTT) conditions. GroEL serves as a loading control. *, non-specific background band.

d, Cell surface exposure of the Type B T9SS substrate SprB assessed by protease protection. Strains expressing a HaloTag fusion between the signal sequence and the final 448 amino

922 acids of SprB (Halo-SprB448) in the indicated genetic backgrounds, were incubated with
923 Proteinase K and the detergent Triton X-100 as indicated. Reactions were stopped
924 immediately (t_0) or after 20 min (t_{20}) and analysed by immunoblotting with HaloTag antibodies.
925 The cytoplasmic protein GroEL serves as both a loading and cell integrity control.
926 **e**, Exemplar trajectories of single fluorophore-labelled HaloTag-SprB adhesin molecules in the
927 indicated backgrounds. The trajectories link the single molecule localizations in successive
928 frames recorded for agarose-immobilised cells and are 2D projections of what is a 3D process.
929 Each trajectory within a cell is shown in a different colour and the segmented outline of the
930 cell is shown in black. For the *gldK*^{C343S} background a cell was chosen to illustrate the observed
931 range of SprB mobility behaviours. See also Supplementary Video 2.
932 **f**, Schematic showing the proposed reactions between the cysteine residues of SprF and GldK
933 (top) and how this is altered in single cysteine SprF variants (bottom). The pink arrows
934 represent attacks by a free cysteine residue on an adjacent disulfide bond. Whether disulfide
935 bond formation between SprF and GldK is reversible under physiological conditions is
936 unknown (indicated by `?').
937 **g,h,** GldK Cys343 is required for Type 9 protein secretion.
938 **g**, Analysis of the secretion of a model Type A substrate protein comprising a fusion between
939 a signal sequence (SS), mCherry (mCh), and a T9SS-targeting C-terminal domain (CTD).
940 Cells were separated into cell and supernatant fractions and analyzed by anti-mCherry
941 immunoblotting. The successively processed forms of the fusion proteins are indicated to the
942 right of the blots. GroEL serves as a loading control.
943 **h**, Secretome analysis. Culture supernatants were separated by SDS-PAGE and stained with
944 Coomassie Blue.
945 **b-e,g,h,** Similar results were obtained for three biological repeats. wt, wild type. Δ*sprA*, a
946 strain missing the T9SS translocon.

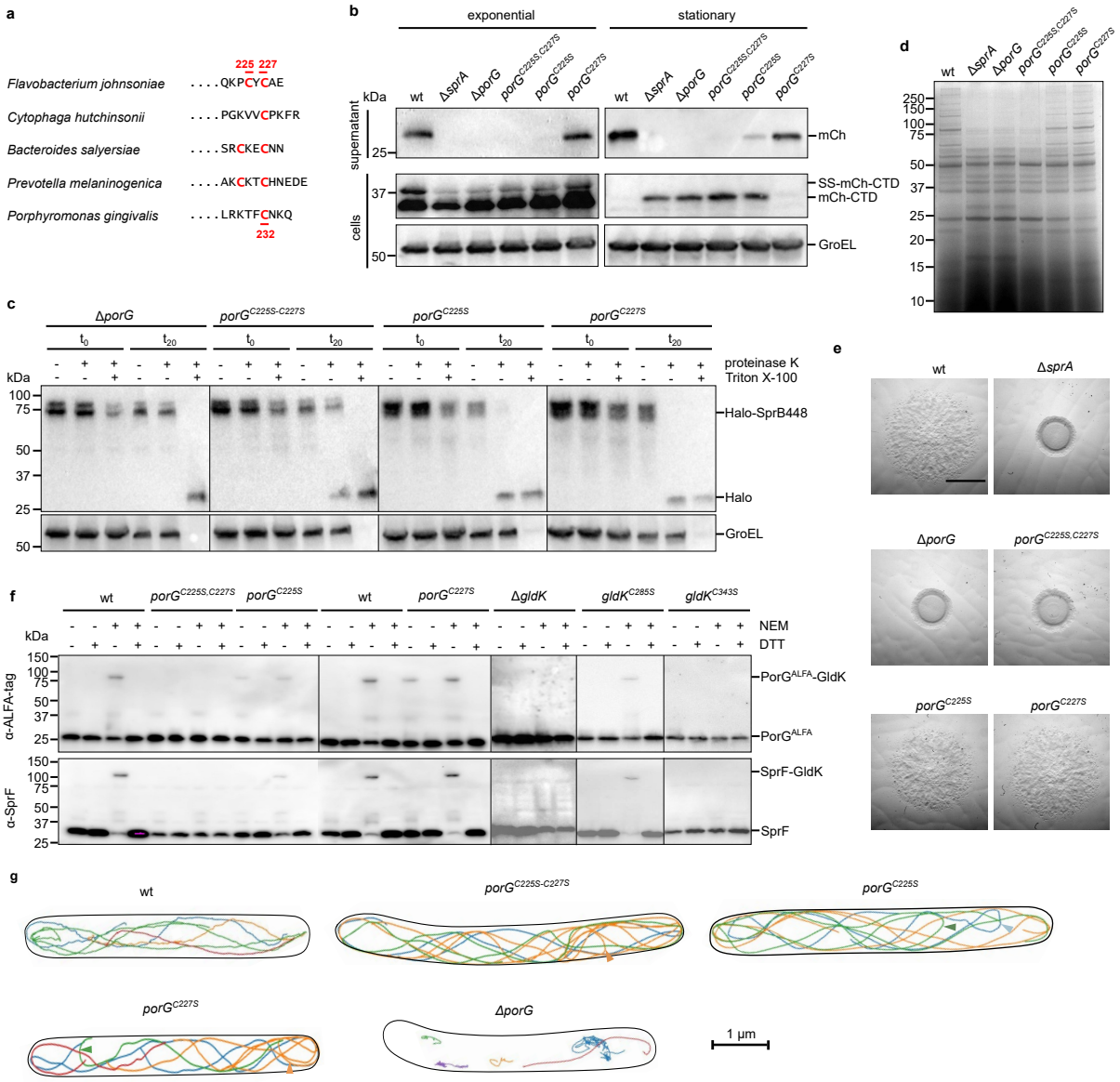

Fig. 4 | *F. johnsoniae* PorG forms a disulfide bond with GldK C343 that is essential for Type 9 protein transport and gliding motility.

a, The periplasmic C-tails of PorG proteins contain cysteine residues. Sequence alignment of representative PorG C-tails from the indicated Bacteroidota species with cysteine residues highlighted.

b-d, The Cys residues of *F. johnsoniae* PorG are required for gliding motility and Type 9 protein transport. wt, wild type. Δ*sprA*, strain missing the T9SS translocon. Similar results were obtained for 3 biological repeats.

b, Analysis of the secretion of a model Type A substrate protein comprising a fusion between a signal sequence (SS), mCherry (mCh), and a T9SS-targeting C-terminal domain (CTD). Cells were grown to exponential or stationary phase as indicated, separated into cell and supernatant fractions, and analyzed by anti-mCherry immunoblotting. The successively

961 processed forms of the fusion proteins are indicated to the right of the blots. GroEL serves as
962 a loading control.
963 **c**, Cell surface exposure of the Type B substrate SprB assessed by protease protection. The
964 specified strains expressing a fusion between HaloTag and the final 448 amino acids of SprB
965 (Halo-SprB$_{448}$) were incubated with Proteinase K and the detergent Triton X-100 as indicated.
966 Reactions were stopped immediately (t_0) or after 20 min (t_{20}) and analysed by immunoblotting
967 with Halotag antibodies. The cytoplasmic protein GroEL serves as a both a loading and cell
968 integrity control.
969 **d,** Secretome analysis. The supernatants of cultures grown to stationary phase were
970 separated by SDS-PAGE and stained with Coomassie Blue.
971 **e,** Spreading (gliding) morphology on agar after 24 h growth. Scale bar, 5mm. See Extended
972 Data Fig. 5a for data at 6 h growth.
973 **f,** PorG is disulfide-bonded to GldK C343. All strains express PorG epitope-tagged by insertion
974 of ALFA-tag in loop 3. Strains were subject to whole cell immunoblotting with the indicated
975 antibodies. Where indicated the cells were pre-treated with NEM. At the SDS-PAGE step
976 samples were run under either non-reducing (- DTT) or reducing (+ DTT) conditions. *, non-
977 specific background band.
978 **g,** Exemplar trajectories of single fluorophore-labelled HaloTag-SprB adhesin molecules in the
979 indicated backgrounds. The trajectories link the single molecule localizations in successive
980 frames recorded for agarose-immobilised cells and are 2D projections of what is a 3D process.
981 Each trajectory within a cell is shown in a different colour and the segmented outline of the
982 cell is shown in black. Un-transported periplasmic SprB molecules have been edited out for
983 clarity. Arrows indicate examples of mid-cell reversals of the SprB trajectories. See also
984 Supplementary Videos 3 and 4.
985 **b-g,** Similar results were obtained from 3 biological repeats. wt, wild type.

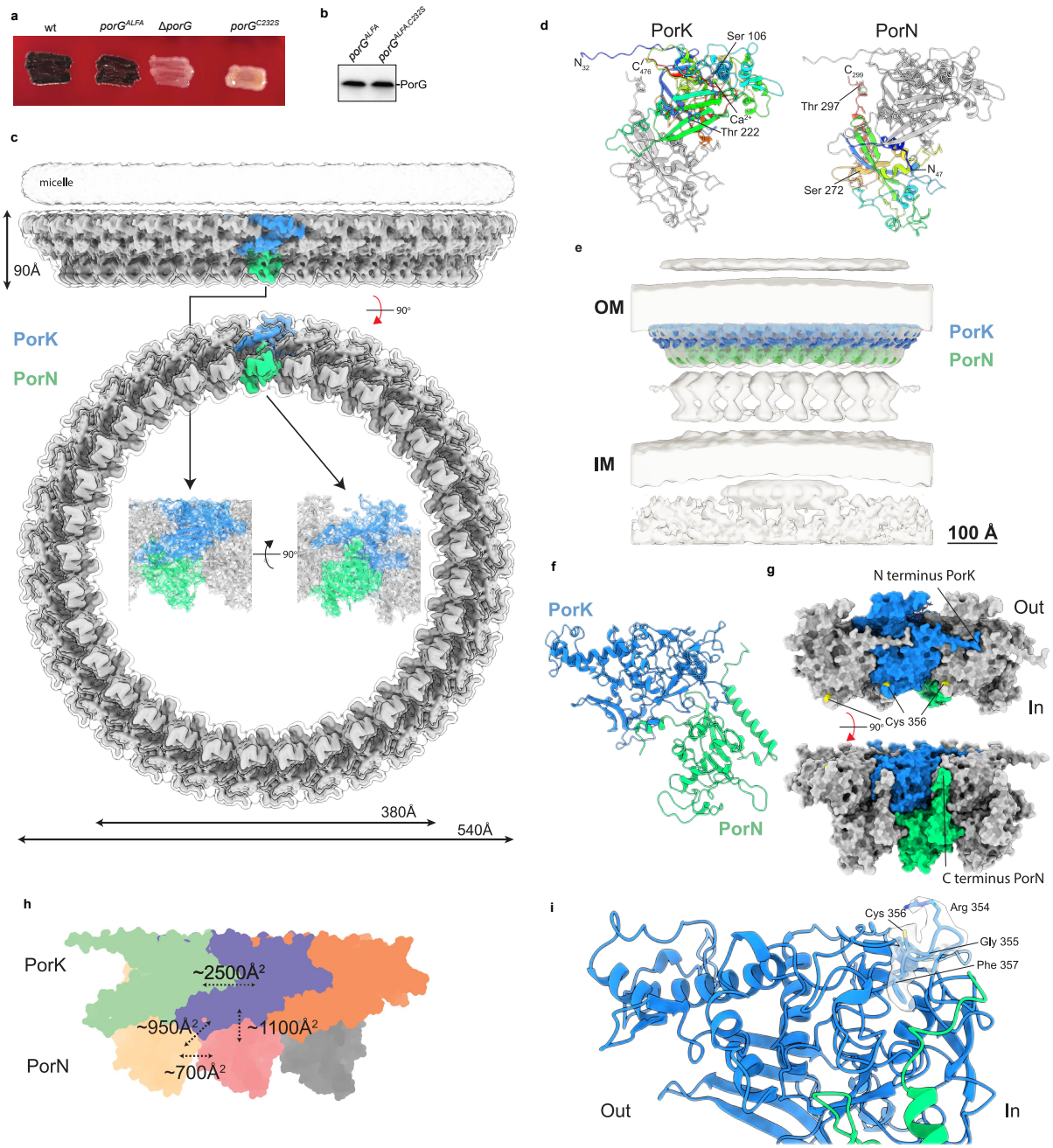

Fig. 5 | Importance of the cysteine residue of *P. gingivalis* PorG and structure of the PorKN Central Hub complex.

a,b, *P. gingivalis* PorG Cys232 is required for T9SS activity. Similar results were obtained from 3 biological repeats. wt, wild type. *porG*^{ALFA}, codes for PorG with an ALFA-tag epitope.

a, Strains containing the indicated *porG* alleles were grown on blood agar.

b, Equivalent strains constructed in a gingipain-deficient background were analysed by whole cell immunoblotting.

c, CryoEM volume for a 33-mer *P. gingivalis* PorKN complex at 4.0 Å resolution viewed from the side and from the periplasm. The inset shows the structure of the repeating PorKN unit

997 obtained at higher (2.4 Å) resolution. The structure is depicted at high contour level (solid
998 representation with a single PorKN unit shown in colour) and at a low contour level
999 (transparent envelope) to visualize the detergent micelle which approximates the position of
1000 the OM.
1001 **d,** Structures of PorK and PorN in cartoon representation and rainbows coloured from N- (blue)
1002 to C-terminus (red), viewed from the inner rim of the PorKN ring and with the OM at Top. The
1003 bound Ca^{2+} ion is shown in atomic sphere representation. Glycosylated serine and threonine
1004 residues are labelled.
1005 **e,** The PorKN structure from **c** (coloured density) placed into the cryoET volume of the complex
1006 resolved previously in intact cells[30] (EMD-24227).
1007 **f,** View of the PorKN heterodimer unit in cartoons representation viewed from within the ring
1008 and with OM at top illustrating the triangular cross-section of the PorKN ring.
1009 **g,** Space-filling model of a PorKN pair and their immediate neighbours viewed from the OM
1010 (Top) and from the outer rim of the PorKN ring with the OM above (Bottom). The position of
1011 the PorG-reactive Cys 356 on PorK is shown (yellow).
1012 **h,** Schematic summarizing the areas buried by the different inter-subunit interfaces of the
1013 PorKN complex. Protomers are oriented as in **d**.
1014 **i,** Structure of the external loop bearing the PorG-reactive cysteine 356 of PorK with density
1015 for the motif overlaid.

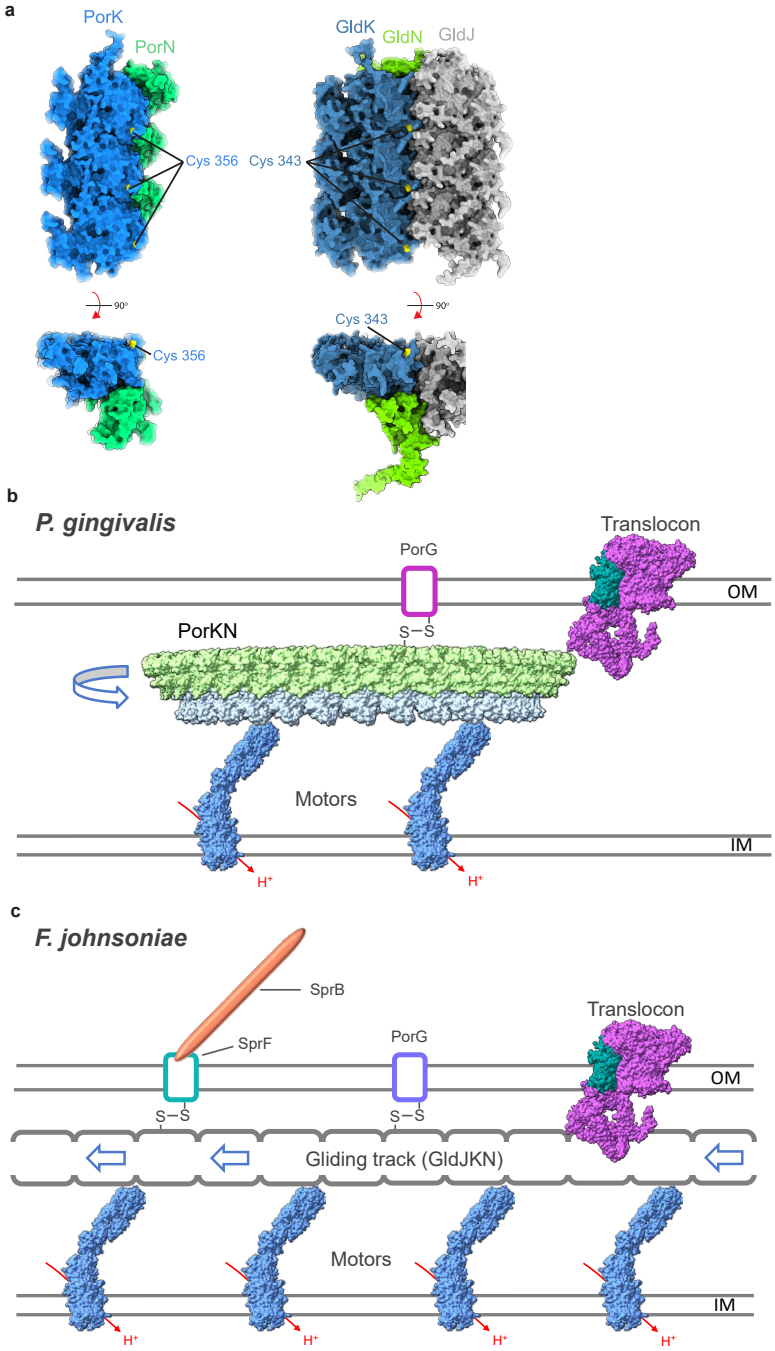

Fig. 6 | A new model for the connection between gliding motility and T9SS protein transport.

a, Comparison of the structure of the *P. gingivalis* PorKN ring oligomer (Left) with an AF3 model for the *F. johnsoniae* GldJKN track oligomer (Right). In each case three adjacent copies of the repeating unit (PorKN or GldJKN) are shown in spacefilling representation viewed from the OM (Top) or in cross-section through the oligomer with the OM at the top (Bottom). The position of the PorG/SprF-interacting cysteines are indicated (yellow).

1025 **b,** Updated model for the organization of the T9SS in the paradigm non-gliding Bacteroidota
1026 *P. gingivalis* based on the findings in this work. The T9SS component PorG is disulfide-linked
1027 to the rotating PorKN Hub complex which energizes the translocon.
1028 **c,** Revised model for the relationship between the gliding motility apparatus and the T9SS in
1029 the paradigm gliding Bacteroidota *F. johnsoniae* based on discoveries in this work. The
1030 adhesin carrier protein SprF and the T9SS component PorG are disulfide-linked to a moving
1031 gliding track composed of GldJ, GldK, and GldN. The translocon receives energetic input from
1032 the gliding track.

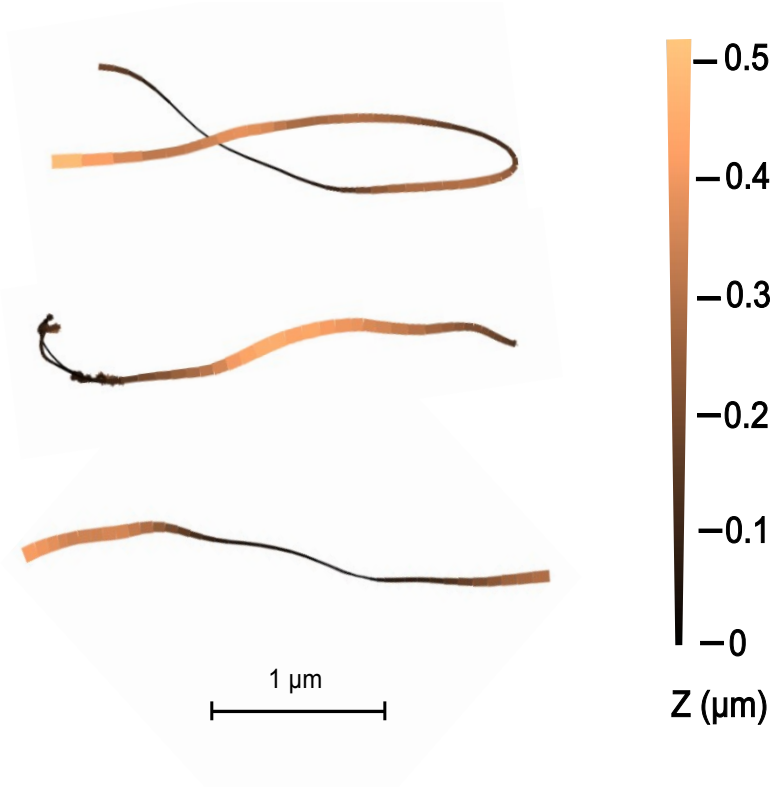

Extended Data Fig. 1 | 3D single particle tracking of fluorescently-tagged SprB adhesin molecules in 3D in SprF cysteine-substituted variants.

The motions of single fluorophore-labelled HaloTag-SprB adhesin molecules were imaged in 3D in agarose-immobilised cells of strains with single and double cysteine substitutions in SprF. The short, apparently directional trajectories present in these cells were extracted and the single molecule localizations in successive frames plotted in xy projection with the relative z position represented by variations in colour and line width as specified in the colour bar. Three representative trajectories are shown. 100 out of 100 such trajectories (from three biological repeats of the three cysteine mutants) where the handedness could be determined showed left-handed helicity consistent with the movement being on the gliding tracks.

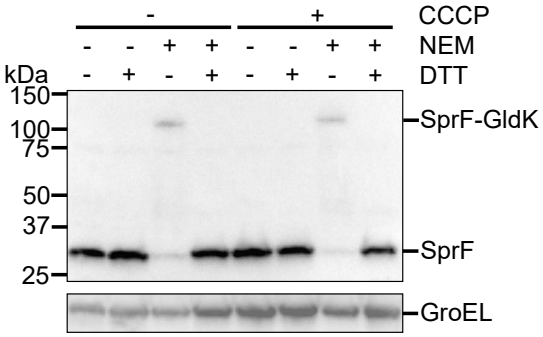

Extended Data Fig. 2 | The disulfide adduct involving SprF is stable to removal of the protonmotive force.

Immunoblots of whole wild type cells. Where indicated the cells were treated with 10 μM of the protonophore carbonyl cyanide *m*-chlorophenyl hydrazone (CCCP) for 20 min before analysis. Where indicated cells were treated with NEM. At the SDS-PAGE step samples were run under either non-reducing (- DTT) or reducing (+ DTT) conditions. GroEL serves as a loading control. Similar results were obtained from three biological repeats.

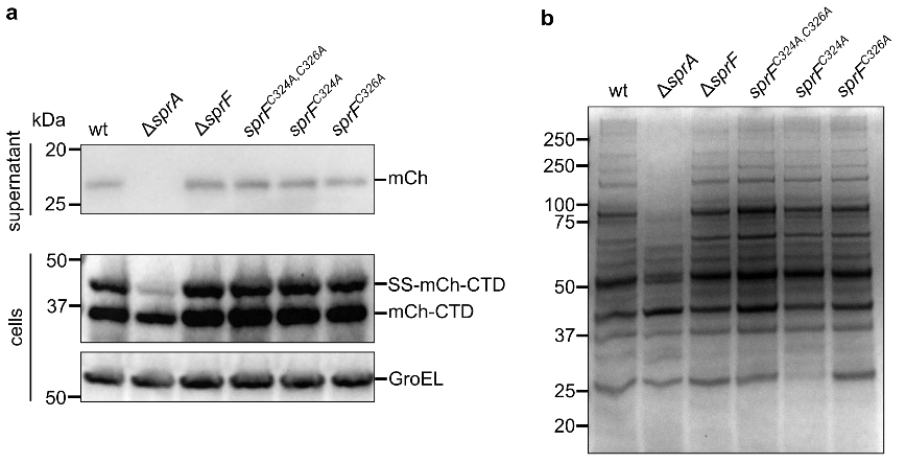

Extended Data Fig. 3 | The GldK-SprF disulfide linkage is not required for the secretion of T9SS Type A substrates. Similar results were obtained from three biological repeats. **a,** Analysis of the secretion of a model Type A substrate protein comprising a fusion between a signal sequence (SS), mCherry (mCh), and a T9SS-targeting C-terminal domain (CTD). whole cell and supernatant samples analyzed by anti-mCherry immunoblotting. The successively processed forms of the fusion proteins are indicated to the right of the blots. The Δ*sprA* strain is missing the T9SS translocon. GroEL serves as a loading control. **b,** Secretome analysis of SprF C-tail cysteine variants. The Δ*sprA* strain is missing the T9SS translocon.

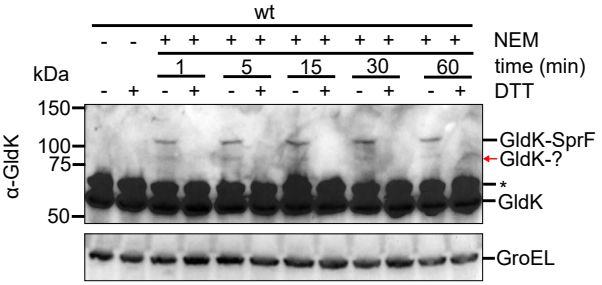

Extended Data Figure 4 | GldK forms disulfide linkages with SprF and another protein.

Wild type cells were subject to whole cell immunoblotting with the specified antisera. Where indicated the cells were pre-treated with NEM for the specified time. At the SDS-PAGE step samples were run under either non-reducing (- DTT) or reducing (+ DTT) conditions. GroEL serves as a loading control. The red arrow indicates a low intensity disulfide-linked adduct band formed by GldK that is additional to the adduct with SprF. *, non-specific background band.

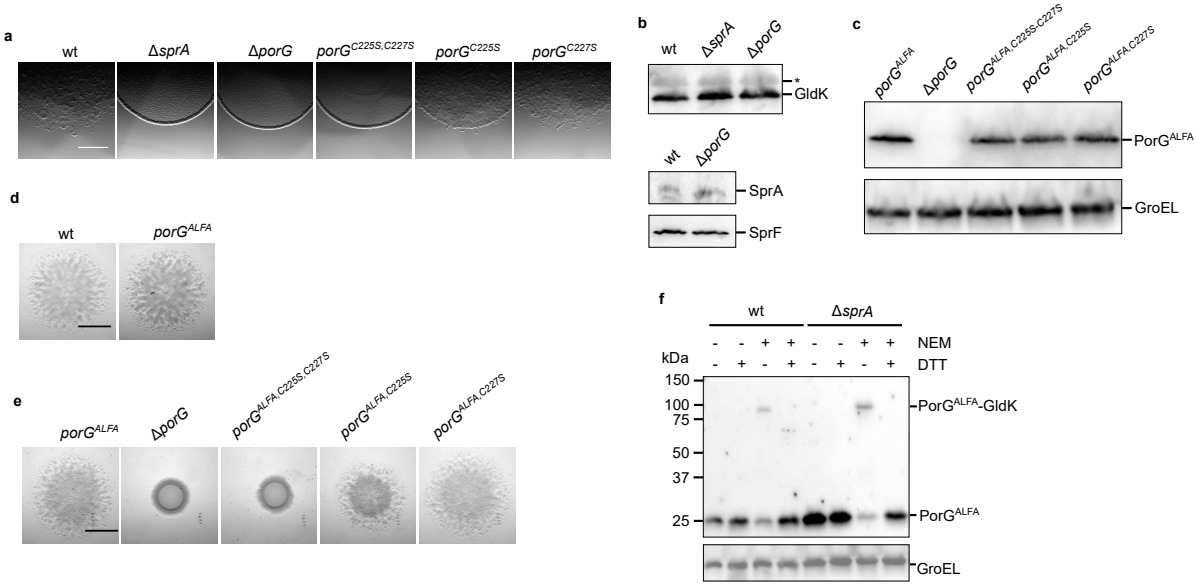

Extended Data Fig. 5 | Characterization of *F. johnsoniae* PorG.

a, Spreading (gliding) morphology of non-tagged PorG cysteine variants at 6 h. Scale bar, 1 mm.

b, *F. johnsoniae* PorG is not required for the expression and stability of the key T9SS and gliding components GldK, SprA, and SprF. Whole cell immunoblotting using antibodies against the indicated proteins. *, non-specific band.

c-e, Insertion of an ALFA-tag into loop 3 does not affect the stability or functionality of *F. johnsoniae* PorG and its variants.

c, Whole cells immunoblotting using ALFA-tag antibodies. GroEL serves as loading control.

d,e, Spreading (gliding) morphology on agar. Scale bar, 5mm.

f, Disulfide bond formation between PorG and GldK does not require T9SS activity. Strains with the indicated mutations were subject to whole cell immunoblotting with ALFA-tag antibodies. Where indicated the cells were pre-treated with NEM. At the SDS-PAGE step samples were run under either non-reducing (- DTT) or reducing (+ DTT) conditions. GroEL serves as a loading control. Δ*sprA*, strain missing the T9SS translocon.

a-f, Similar results were obtained from 3 biological repeats. wt, wild type.

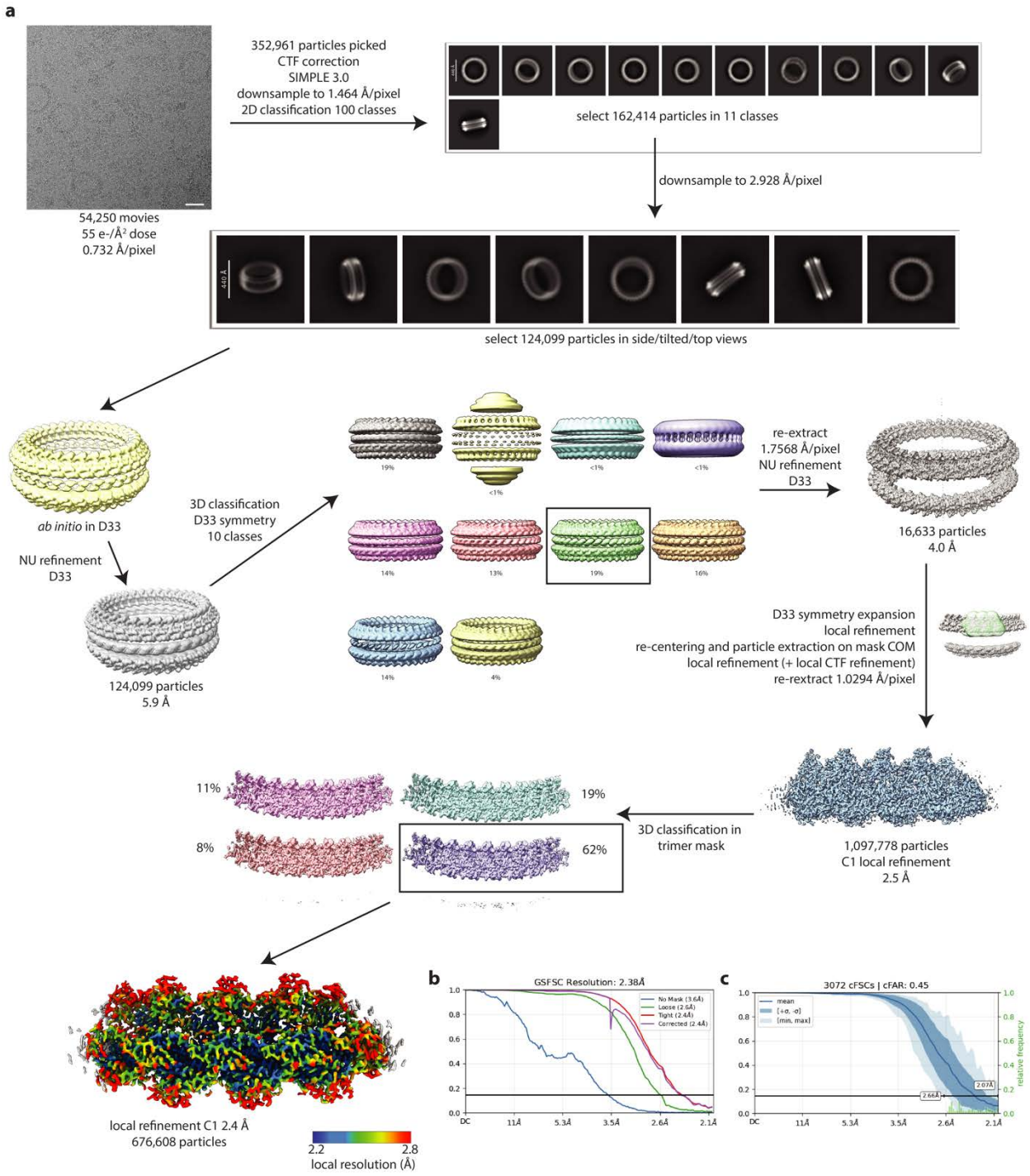

Extended Data Fig. 6 | Cryo-EM Workflow for the *P. gingivalis* PorKN complex structure. **a**, Image processing workflow, including the local resolution estimate of the volume. Micrograph scale bar is 300 Å.

b, Gold-standard Fourier Shell Correlation (FSC) curves used for global resolution estimation.

c, Conical FSC (cFSC) plot assessing directional signal content.

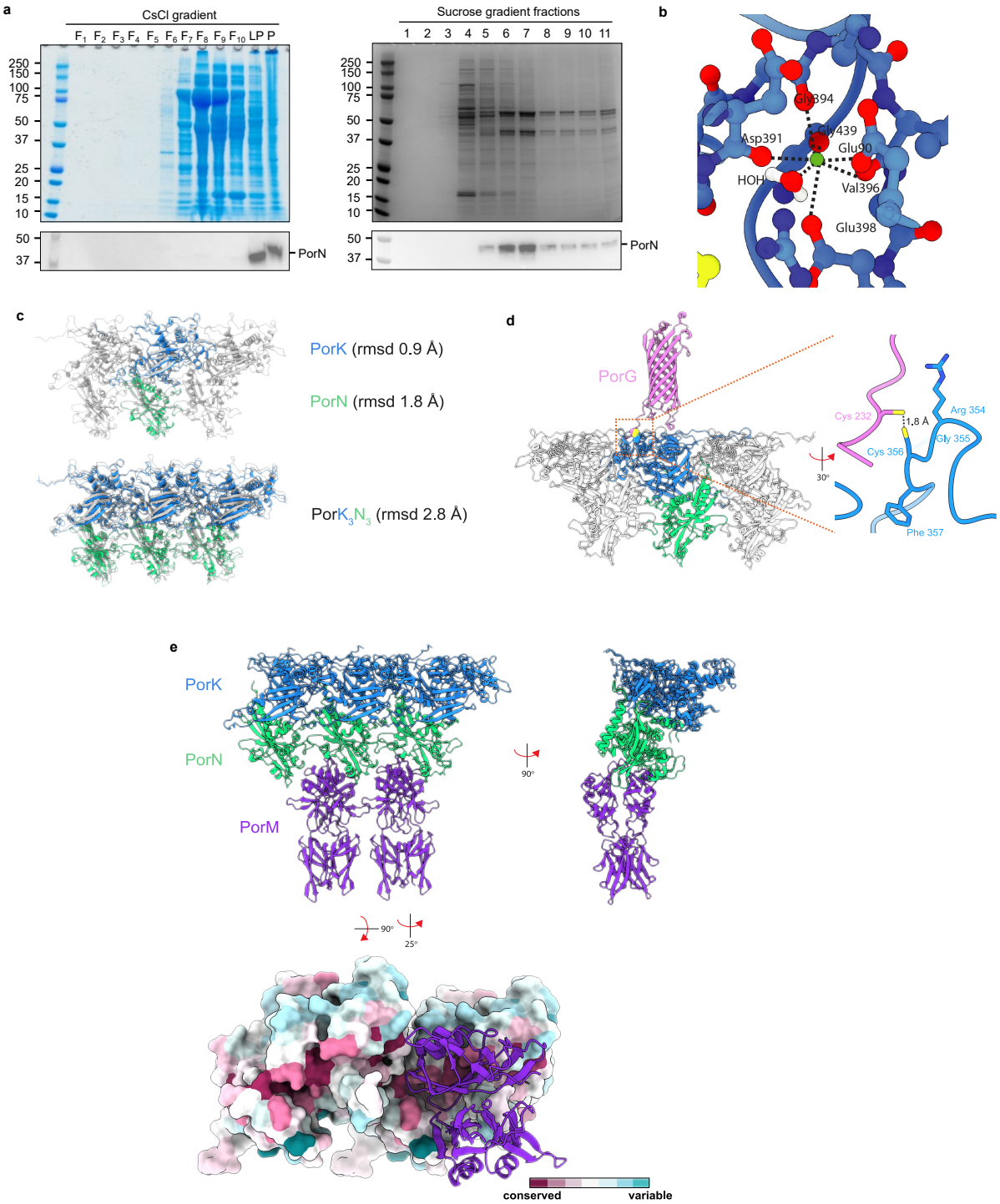

Extended Data Fig. 7 | Further information on the *P. gingivalis* PorKN complex.

a, Purification of the PorKN complex for structural analysis. The successive CsCl and sucrose density gradient steps of an exemplar preparation are shown. Coomassie Blue stained SDS-PAGE gels with corresponding anti-PorN immunoblots below. Fractions (F) are numbered from the tops of the gradients. P, pellet; LP, loose pellet. Fraction LP from the CsCl was loaded onto the sucrose gradient from which fractions F6 and F7 were pooled and used for structure determination.

1108 **b,** The Ca^{2+} ion binding site in PorK with the metal ion (green) and co-ordinating ligands shown
1109 as atomic spheres.

1110 **c,** AF3 reliably models the PorKN oligomer. AF3 models (coloured cartoons) of the isolated
1111 PorK and PorN subunits (Top) or of the complex between three PorKN units (Bottom) are
1112 superpositioned on a three PorKN unit section of the experimental structure (grey cartoons)
1113 with the indicated RMSDs.

1114 **d,** AF3 model in cartoons representation for the complex formed between PorG and the PorKN
1115 ring. The model contains one copy of PorG and three copies of the PorKN unit. No protein-
1116 protein protein contacts are predicted beyond the intersubunit disulfide linkage.

1117 **e,** AF3 model for the complex formed between the distal ends of the PorM motor arms and the
1118 PorKN ring. The model contains three copies of the PorKN unit and four copies of the D3-D4
1119 fragment of PorM. Note that each PorM arm is a homodimer. (Top) Two views of the model in
1120 cartoons representation. (Bottom) The model viewed from the periplasm but with the PorKN
1121 units shown in spacefilling representation and coloured by sequence conservation using
1122 Consurf[63]. One of the PorM homodimer arms has been removed to allow the PorM interaction
1123 surface on PorKN to be inspected. The remaining PorM homodimer arm is shown in cartoons
1124 representation with the upper PorM subunit forming the potential specific interaction with
1125 PorKN.

1126 # References

1127

1128 1 Veith, P. D., Glew, M. D., Gorasia, D. G. & Reynolds, E. C. Type IX secretion: the
1129 generation of bacterial cell surface coatings involved in virulence, gliding motility and
1130 the degradation of complex biopolymers. *Mol Microbiol* **106**, 35-53 (2017).
1131 https://doi.org:10.1111/mmi.13752

1132 2 Lasica, A. M., Ksiazek, M., Madej, M. & Potempa, J. The Type IX Secretion System
1133 (T9SS): Highlights and Recent Insights into Its Structure and Function. *Front Cell Infect*
1134 *Microbiol* **7**, 215 (2017). https://doi.org:10.3389/fcimb.2017.00215

1135 3 Veith, P. D., Glew, M. D., Gorasia, D. G., Cascales, E. & Reynolds, E. C. The Type IX
1136 Secretion System and Its Role in Bacterial Function and Pathogenesis. *J Dent Res*
1137 **101**, 374-383 (2022). https://doi.org:10.1177/00220345211051599

1138 4 Paillat, M., Lunar Silva, I., Cascales, E. & Doan, T. A journey with type IX secretion
1139 system effectors: selection, transport, processing and activities. *Microbiology*
1140 *(Reading)* **169** (2023). https://doi.org:10.1099/mic.0.001320

1141 5 McBride, M. J. Bacteroidetes Gliding Motility and the Type IX Secretion System.
1142 *Microbiol Spectr* **7** (2019). https://doi.org:10.1128/microbiolspec.PSIB-0002-2018

1143 6 Li, Y. *et al.* Identification of trypsin-degrading commensals in the large intestine. *Nature*
1144 **609**, 582-589 (2022). https://doi.org:10.1038/s41586-022-05181-3

1145 7 Lauber, F., Deme, J. C., Lea, S. M. & Berks, B. C. Type 9 secretion system structures
1146 reveal a new protein transport mechanism. *Nature* **564**, 77-82 (2018).
1147 https://doi.org:10.1038/s41586-018-0693-y

1148 8 Lauber, F. *et al.* Structural insights into the mechanism of protein transport by the Type
1149 9 Secretion System translocon. *Nat Microbiol* (2024). https://doi.org:10.1038/s41564-
1150 024-01644-7

1151 9 Kulkarni, S. S., Zhu, Y., Brendel, C. J. & McBride, M. J. Diverse C-Terminal Sequences
1152 Involved in Flavobacterium johnsoniae Protein Secretion. *J Bacteriol* **199** (2017).
1153 https://doi.org:10.1128/JB.00884-16

1154 10 Glew, M. D. *et al.* PorV is an Outer Membrane Shuttle Protein for the Type IX Secretion
1155 System. *Sci Rep* **7**, 8790 (2017). https://doi.org:10.1038/s41598-017-09412-w

1156 11 Kulkarni, S. S., Johnston, J. J., Zhu, Y., Hying, Z. T. & McBride, M. J. The Carboxy-
1157 Terminal Region of Flavobacterium johnsoniae SprB Facilitates Its Secretion by the
1158 Type IX Secretion System and Propulsion by the Gliding Motility Machinery. *J Bacteriol*
1159 **201** (2019). https://doi.org:10.1128/JB.00218-19

1160 12 Gorasia, D. G. *et al.* Type B CTD Proteins Secreted by the Type IX Secretion System
1161 Associate with PorP-like Proteins for Cell Surface Anchorage. *Int J Mol Sci* **23** (2022).
1162 https://doi.org:10.3390/ijms23105681

1163 13 Wadhwa, N. & Berg, H. C. Bacterial motility: machinery and mechanisms. *Nat Rev*
1164 *Microbiol* **20**, 161-173 (2022). https://doi.org:10.1038/s41579-021-00626-4

1165 14 Nelson, S. S., Bollampalli, S. & McBride, M. J. SprB is a cell surface component of the
1166 Flavobacterium johnsoniae gliding motility machinery. *J Bacteriol* **190**, 2851-2857
1167 (2008). https://doi.org:10.1128/JB.01904-07

1168 15 Nakane, D., Sato, K., Wada, H., McBride, M. J. & Nakayama, K. Helical flow of surface
1169 protein required for bacterial gliding motility. *Proc Natl Acad Sci U S A* **110**, 11145-
1170 11150 (2013). https://doi.org:10.1073/pnas.1219753110

1171 16 Shibata, S. *et al.* Filamentous structures in the cell envelope are associated with
1172 bacteroidetes gliding machinery. *Commun Biol* **6**, 94 (2023).
1173 https://doi.org:10.1038/s42003-023-04472-3

17 Miller, H., Kjaer, A., Coppola, S., Jones, R., Berks, B.C., and Berry, R.M. *Architecture of the Bacteroidota gliding motility machinery revealed by 3D tracking of adhesin movements* (2025).

18 Shrivastava, A., Roland, T. & Berg, H. C. The Screw-Like Movement of a Gliding Bacterium Is Powered by Spiral Motion of Cell-Surface Adhesins. *Biophys J* **111**, 1008-1013 (2016). https://doi.org:10.1016/j.bpj.2016.07.043

19 Wada, H., Nakane, D. & Chen, H. Y. Bidirectional bacterial gliding motility powered by the collective transport of cell surface proteins. *Phys Rev Lett* **111**, 248102 (2013). https://doi.org:10.1103/PhysRevLett.111.248102

20 Rhodes, R. G., Nelson, S. S., Pochiraju, S. & McBride, M. J. Flavobacterium johnsoniae sprB is part of an operon spanning the additional gliding motility genes sprC, sprD, and sprF. *J Bacteriol* **193**, 599-610 (2011). https://doi.org:10.1128/JB.01203-10

21 Braun, T. F. & McBride, M. J. Flavobacterium johnsoniae GldJ is a lipoprotein that is required for gliding motility. *J Bacteriol* **187**, 2628-2637 (2005). https://doi.org:10.1128/JB.187.8.2628-2637.2005

22 Shrivastava, A. & Berg, H. C. A molecular rack and pinion actuates a cell-surface adhesin and enables bacterial gliding motility. *Sci Adv* **6**, eaay6616 (2020). https://doi.org:10.1126/sciadv.aay6616

23 Trivedi, A. M., J. A.; Henderson, E. C.; Singharoy, A.; Shrivastava, A. A membrane-associated conveyor belt controls the rotational direction of the bacterial type 9 secretion system. *bioRxiv* (2025). https://doi.org: https://doi.org/10.1101/2024.09.23.614571

24 Sato, K. *et al.* A protein secretion system linked to bacteroidete gliding motility and pathogenesis. *Proc Natl Acad Sci U S A* **107**, 276-281 (2010). https://doi.org:10.1073/pnas.0912010107

25 Hennell James, R. *et al.* Structure and mechanism of the proton-driven motor that powers type 9 secretion and gliding motility. *Nat Microbiol* **6**, 221-233 (2021). https://doi.org:10.1038/s41564-020-00823-6

26 Shrivastava, A., Johnston, J. J., van Baaren, J. M. & McBride, M. J. Flavobacterium johnsoniae GldK, GldL, GldM, and SprA are required for secretion of the cell surface gliding motility adhesins SprB and RemA. *J Bacteriol* **195**, 3201-3212 (2013). https://doi.org:10.1128/JB.00333-13

27 Leone, P. *et al.* Type IX secretion system PorM and gliding machinery GldM form arches spanning the periplasmic space. *Nat Commun* **9**, 429 (2018). https://doi.org:10.1038/s41467-017-02784-7

28 Rieu, M., Krutyholowa, R., Taylor, N. M. I. & Berry, R. M. A new class of biological ion-driven rotary molecular motors with 5:2 symmetry. *Front Microbiol* **13**, 948383 (2022). https://doi.org:10.3389/fmicb.2022.948383

29 Gorasia, D. G. *et al.* Structural Insights into the PorK and PorN Components of the Porphyromonas gingivalis Type IX Secretion System. *PLoS Pathog* **12**, e1005820 (2016). https://doi.org:10.1371/journal.ppat.1005820

30 Song, L. *et al.* A unique bacterial secretion machinery with multiple secretion centers. *Proc Natl Acad Sci U S A* **119**, e2119907119 (2022). https://doi.org:10.1073/pnas.2119907119

31 Gorasia, D. G. C., G.; Seers, C.A.; Butler, C.A.; Heath, J.E.; Glew, M.D.; McBride, M.J.; Subramanian, P.; Kjær, A.; Jensen, G.J.; Veith, P.D.; Reynolds, E.C. In situ structure and organisation of the type IX secretion system. *bioRxiv* (2020).

32 Braun, T. F., Khubbar, M. K., Saffarini, D. A. & McBride, M. J. Flavobacterium johnsoniae gliding motility genes identified by mariner mutagenesis. *J Bacteriol* **187**, 6943-6952 (2005). https://doi.org:10.1128/JB.187.20.6943-6952.2005

33 Abramson, J. *et al.* Accurate structure prediction of biomolecular interactions with AlphaFold 3. *Nature* **630**, 493-500 (2024). https://doi.org:10.1038/s41586-024-07487-w

34 Alvarez, B., Secades, P., Prieto, M., McBride, M. J. & Guijarro, J. A. A mutation in Flavobacterium psychrophilum tlpB inhibits gliding motility and induces biofilm formation. *Appl Environ Microbiol* **72**, 4044-4053 (2006). https://doi.org:10.1128/AEM.00128-06

35 Zhao, D. *et al.* A Disulfide Oxidoreductase (CHU_1165) Is Essential for Cellulose Degradation by Affecting Outer Membrane Proteins in Cytophaga hutchinsonii. *Appl Environ Microbiol* **86** (2020). https://doi.org:10.1128/AEM.02789-19

36 Kjaer, A. *Investigating bacteroidetes gliding motility*, University of Oxford, (2022).

37 Naito, M., Tominaga, T., Shoji, M. & Nakayama, K. PGN_0297 is an essential component of the type IX secretion system (T9SS) in Porphyromonas gingivalis: Tn-seq analysis for exhaustive identification of T9SS-related genes. *Microbiol Immunol* **63**, 11-20 (2019). https://doi.org:10.1111/1348-0421.12665

38 Ono, S. *et al.* Construction and Characterization of a PGN_0297 Mutant of Porphyromonas gingivalis: Evidence of the Contribution of PGN_0297 to Gingipain Activity. *Acta Med Okayama* **73**, 315-323 (2019). https://doi.org:10.18926/AMO/56933

39 Nakayama, K. Porphyromonas gingivalis and related bacteria: from colonial pigmentation to the type IX secretion system and gliding motility. *J Periodontal Res* **50**, 1-8 (2015). https://doi.org:10.1111/jre.12255

40 Johnson, S. *et al.* Molecular structure of the intact bacterial flagellar basal body. *Nat Microbiol* **6**, 712-721 (2021). https://doi.org:10.1038/s41564-021-00895-y

41 Johnson, S. *et al.* Structural basis of directional switching by the bacterial flagellum. *Nat Microbiol* **9**, 1282-1292 (2024). https://doi.org:10.1038/s41564-024-01630-z

42 Dierks, T. *et al.* Molecular basis for multiple sulfatase deficiency and mechanism for formylglycine generation of the human formylglycine-generating enzyme. *Cell* **121**, 541-552 (2005). https://doi.org:10.1016/j.cell.2005.03.001

43 Fuchsbauer, O., Lunar Silva, I., Cascales, E., Roussel, A. & Leone, P. Structural and functional analyses of the Porphyromonas gingivalis type IX secretion system PorN protein. *J Biol Chem* **298**, 101618 (2022). https://doi.org:10.1016/j.jbc.2022.101618

44 Vincent, M. S. *et al.* Dynamic proton-dependent motors power type IX secretion and gliding motility in Flavobacterium. *PLoS Biol* **20**, e3001443 (2022). https://doi.org:10.1371/journal.pbio.3001443

45 Vincent, M. S. *et al.* Characterization of the Porphyromonas gingivalis Type IX Secretion Trans-envelope PorKLMNP Core Complex. *J Biol Chem* **292**, 3252-3261 (2017). https://doi.org:10.1074/jbc.M116.765081

46 Johnston, J. J., Shrivastava, A. & McBride, M. J. Untangling Flavobacterium johnsoniae Gliding Motility and Protein Secretion. *J Bacteriol* **200** (2018). https://doi.org:10.1128/JB.00362-17

47 Worrall, L. J., Majewski, D. D. & Strynadka, N. C. J. Structural Insights into Type III Secretion Systems of the Bacterial Flagellum and Injectisome. *Annual review of microbiology* **77**, 669-698 (2023). https://doi.org:10.1146/annurev-micro-032521-025503

48 McBride, M. J. & Kempf, M. J. Development of techniques for the genetic manipulation of the gliding bacterium Cytophaga johnsonae. *J Bacteriol* **178**, 583-590 (1996).

49 Liu, J., McBride, M. J. & Subramaniam, S. Cell surface filaments of the gliding bacterium Flavobacterium johnsoniae revealed by cryo-electron tomography. *J Bacteriol* **189**, 7503-7506 (2007). https://doi.org:10.1128/JB.00957-07

50 Agarwal, S., Hunnicutt, D. W. & McBride, M. J. Cloning and characterization of the Flavobacterium johnsoniae (Cytophaga johnsonae) gliding motility gene, gldA. *Proc Natl Acad Sci U S A* **94**, 12139-12144 (1997).

51 Gibson, D. G. *et al.* Enzymatic assembly of DNA molecules up to several hundred kilobases. *Nat Methods* **6**, 343-345 (2009). https://doi.org:10.1038/nmeth.1318

52 Zhu, Y. *et al.* Genetic analyses unravel the crucial role of a horizontally acquired alginate lyase for brown algal biomass degradation by Zobellia galactanivorans. *Environ Microbiol* **19**, 2164-2181 (2017). https://doi.org:10.1111/1462-2920.13699

53 Stafford, P. *et al.* Gingipain-dependent degradation of mammalian target of rapamycin pathway proteins by the periodontal pathogen Porphyromonas gingivalis during invasion. *Mol Oral Microbiol* **28**, 366-378 (2013). https://doi.org:10.1111/omi.12030

54 Nelson, S. S., Glocka, P. P., Agarwal, S., Grimm, D. P. & McBride, M. J. Flavobacterium johnsoniae SprA is a cell surface protein involved in gliding motility. *J Bacteriol* **189**, 7145-7150 (2007). https://doi.org:10.1128/JB.00892-07

55 Ovesny, M., Krizek, P., Borkovec, J., Svindrych, Z. & Hagen, G. M. ThunderSTORM: a comprehensive ImageJ plug-in for PALM and STORM data analysis and super-resolution imaging. *Bioinformatics* **30**, 2389-2390 (2014). https://doi.org:10.1093/bioinformatics/btu202

56 Gorasia, D. G., Hanssen, E., Veith, P. D. & Reynolds, E. C. Structural Characterization of the Type IX Secretion System in Porphyromonas gingivalis. *Methods Mol Biol* **2210**, 113-121 (2021). https://doi.org:10.1007/978-1-0716-0939-2_11

57 Caesar, J. *et al.* SIMPLE 3.0. Stream single-particle cryo-EM analysis in real time. *J Struct Biol X* **4**, 100040 (2020). https://doi.org:10.1016/j.yjsbx.2020.100040

58 Punjani, A., Zhang, H. & Fleet, D. J. Non-uniform refinement: adaptive regularization improves single-particle cryo-EM reconstruction. *Nat Methods* **17**, 1214-1221 (2020). https://doi.org:10.1038/s41592-020-00990-8

59 Brown, A. *et al.* Tools for macromolecular model building and refinement into electron cryo-microscopy reconstructions. *Acta Crystallogr D Biol Crystallogr* **71**, 136-153 (2015). https://doi.org:10.1107/S1399004714021683

60 Afonine, P. V. *et al.* Real-space refinement in PHENIX for cryo-EM and crystallography. *Acta Crystallogr D Struct Biol* **74**, 531-544 (2018). https://doi.org:10.1107/S2059798318006551

61 Williams, C. J. *et al.* MolProbity: More and better reference data for improved all-atom structure validation. *Protein Sci* **27**, 293-315 (2018). https://doi.org:10.1002/pro.3330

62 Pettersen, E. F. *et al.* UCSF ChimeraX: Structure visualization for researchers, educators, and developers. *Protein Sci* **30**, 70-82 (2021). https://doi.org:10.1002/pro.3943

63 Ashkenazy, H. *et al.* ConSurf 2016: an improved methodology to estimate and visualize evolutionary conservation in macromolecules. *Nucleic Acids Res* **44**, W344-350 (2016). https://doi.org:10.1093/nar/gkw408